Development and validation of a portal dose prediction model

van Elmpt, W.J.C.

Award date:
2004

TU/e technische universiteit eindhoven

Technische Universiteit Eindhoven
Faculteit Technische Natuurkunde
Magnetic Resonance Laboratories /
Transport in Permeable Media
P.O. Box 513
NL-5600 MB Eindhoven

MAASTRO

Maastricht Radiation Oncology
MAASTRO CLINIC
Klinisch Fysische Groep

P.O. Box 4446
NL-6401 CX Heerlen

Development and validation of a portal dose prediction model.

W.J.C. van Elmpt

MRL/TPM 2004 - 02

October 2004

Masters thesis	:	November 2003 – October 2004.
Advisors MAASTRO CLINIC	:	ir. S.M.J.J.G. Nijsten dr. ir. A.W.H. Minken
Supervisor TU/e	:	prof. dr. ir. P.F.F. Wijn

Abstract

Introduction: The verification of a full three-dimensional dose distribution inside the patient during external radiotherapy is the ultimate goal of in-vivo dosimetry. Electronic portal imaging devices (EPIDs) are capable of making a two-dimensional dose distribution behind the patient, also called portal dosimetry. The aim of this report is to give a detailed description of this portal dose behind a patient and analyse the various factors that influence this dose distribution.

Methods: A model based on a pencil beam concept is developed to predict the portal dose behind a patient. The portal dose is composed of primary and scattered (patient) dose. The model takes into account the attenuation of the primary dose and the creation of the scatter exiting the patient by evaluating the radiological thickness. The model employs phantom measurements as input parameters. To assess the accuracy of the model, both homogeneous as well as inhomogeneous phantom measurements are performed. Also actual patient data are used.

Results: In case of homogeneous phantoms the model is able to predict the portal dose within 2% of the measured portal dose. For inhomogeneous phantoms with the center-of-mass coinciding with the isocenter the error is below 2%, deviations from this center-of-mass criterium results in an approximation of the predicted portal dose. For an actual treatment of a breast cancer patient the predicted dose was within 3% of the measured dose.

Conclusion: The model shows good agreement with the measurements for homogeneous and highly inhomogeneous phantoms. The model can also be used to extract the primary dose from measured portal images, which will be the first step towards full three-dimensional dose reconstruction.

Contents

Abbreviations and Symbols

Frequently used abbreviations

2-D	two-dimensional
3-D	three-dimensional
CT	computed tomography
DRR	digitally reconstructed radiograph
EHP	equivalent homogeneous phantom
EPID	electronic portal imaging device
HWHM	half width at half maximum
linac	linear accelerator
MDD	midplane-to-detector distance
PBSK	pencil beam scatter kernel
PDI	portal dose image
PS	polystyrene
SDD	source-to-detector distance
SPR	scatter-to-primary ratio
SSD	source-to-surface distance
TPS	treatment planning system

Frequently used symbols

$\mathbf{r} = (x, y)$	coordinate in portal plane
$r = \lvert\mathbf{r}\rvert = \sqrt{x^2 + y^2})$	off-axis distance in portal plane
E	photon energy
L	midplane-to-detector distance
t	radiological thickness
$\mu(r, t)$	effective attenuation coefficient
$O(\mathbf{r})$	open beam dose distribution in portal plane
$I(\mathbf{r}, t)$	total dose distribution in portal plane
$P(\mathbf{r}, t)$	primary dose distribution in portal plane
$S(\mathbf{r}, t)$	scattered dose distribution in portal plane
$T(\mathbf{r}, t)$	total transmission in portal plane
$T^P(\mathbf{r}, t)$	primary transmission in portal plane
$T^S(\mathbf{r}, t)$	scattered transmission in portal plane
$K_L(t, r)$	scatter kernel for midplane-to-detector distance L
$K(t, r)$	scatter kernel for midplane-to-detector distance in fitting geometry
$c_1(t),\ c_2(t),\ c_3(t)$	fitting coefficients

General Introduction

MAASTRO CLINIC is a radiotherapy center for the most southern part of the Netherlands. Radiotherapy is the modality for treating cancer with high energetic radiation to destroy tumor cells inside the human body. The aim of the treatment is to deliver a homogeneous dose prescribed by the physician to tumor cells while keeping the dose to healthy tissue as low as possible. Hence, the accuracy of treatment delivery should be high. The effect of radiation on human tissue is that cells can be damaged or destroyed. Another fact supporting the use of radiation to kill cells, is that healthy cells recover faster from damage due to radiation than tumor cells. Also the dose-effect relation for tumor cells is different from that for healthy tissue. This all requires a high precision treatment with small tolerances. Dosimetric errors should be smaller than a few percent and spatial errors should not exceed a few millimeter. Hence, quality control procedures are necessary.

Besides technical quality control of the treatment devices, also the dose actually delivered to the patient is verified in MAASTRO CLINIC: in-vivo dosimetry. This report describes the first steps towards the ultimate goal of in-vivo dosimetry: a full three-dimensional dose reconstruction.

Three-dimensional dose reconstruction uses the relation between measured dose distributions behind a patient (transmission dose) and the actual dose deposition inside the patient. An accurate description and understanding of this transmission dose is therefore mandatory. This report gives a detailed analysis of the various factors that influence the transmission dose, as a first step towards full three-dimensional dose reconstruction.

Aim of this study

The aim of this study is to give a detailed analysis of the dose behind a patient. This dose can be measured but also a model is developed to predict this dose. The various factors influencing this dose distribution are discussed as well as the accuracy of the prediction that can be achieved. The model is tested on both phantom as well as clinical data. The criteria for the model are chosen such that not only the dose can be predicted with a high accuracy (<2% deviations from the measurement) but that the data can also be used as input for a three-dimensional dose reconstruction method.

Report outline

In chapter 1, an introduction to in-vivo dosimetry is given, as well as an overview of the various methods and equipment. In chapter 2 a framework of the physics involved in radiotherapy is discussed. Chapter 3 qualitatively describes the various factors influencing the transmission dose and some methods described in literature to predict this dose. In chapter 4, a new model is developed to predict the portal dose that can also be used for a three-dimensional dose reconstruction method. In chapter 5 the input parameters for the model are derived. Chapter 6 assesses the accuracy of the model experimentally by using homogeneous and inhomogeneous phantoms. Also a clinical data is example is given. Finally, a general discussion and conclusions are given in chapter 7.

Chapter 1

In-Vivo Dosimetry in Radiotherapy

Besides surgery and chemotherapy, radiotherapy is an important modality used in the treatment of cancer. The aim of radiotherapy is to deliver a homogeneous dose to a tumor volume and to keep the dose to normal tissue as low as possible. Radiotherapy can be divided in two main areas: teletherapy and brachytherapy[1]. In teletherapy, high energetic x-rays or electrons, generated with linear accelerators (linacs), are most often used for irradiation. The treatment (tumor) volume is usually localized using a computed tomography (CT) scan. A treatment planning system (TPS) calculates the dose distribution inside the patient that is produced by the linear accelerator. Brachytherapy on the other hand uses sealed radio-active sources that are placed directly inside the tumor volume. This gives a very localized dose distribution around the radioactive sources and a very low dose to healthy tissue.

1.1 In-vivo dosimetry

In-vivo dosimetry is a method of checking if the prescribed dose is actually delivered to the patient. Various methods and equipment are developed for this verification. Point measurements can be performed by using diodes, thermoluminescence dosimeters (TLD) or metal oxide semiconductor field effect transistors (MOSFET) detectors. All these detectors can be positioned on the patient skin or in body cavities allowing entrance and exit dose measurements. An extensive overview of the characteristics and the use of diodes and TLDs in clinical practice is given by Essers and Mijnheer [1]. Entrance dose measurements are usually performed to detect errors in the output of the treatment device; exit dose measurements can be done to detect errors in the dose calculation algorithm of the TPS.

However, the ultimate goal of in-vivo dosimetry is not only to check the delivered dose at specific points but to make a full three-dimensional (3-D) dose reconstruction inside the patient. Electronic portal imaging devices (EPID) can be used for this purpose because they are capable of generating a two-dimensional (2-D) portal dose image (PDI) behind a patient. For in-vivo dosimetry, this portal dose distribution must in some way be related to the patient. As a first step towards a full 3-D dose reconstruction the portal dose can be used to derive 2-D exit or midplane dose distributions inside the patient.

In this chapter, the methods presented in literature to derive these 2-D dose distributions are explained (section 1.2), as well as the first steps towards a full 3-D dose reconstruction (section 1.3).

[1]The Greek word 'brachy' means close or nearby and is the opposite of 'tele' which means far or at a distance.

1.2 Two-dimensional dose reconstruction

Various approaches are presented in literature for the 2-D verification of the dose during treatment. The portal dose image can be predicted in advance and compared with the image acquired during treatment, but also exit dose and midplane dose can be estimated from portal dose images.

Portal dose prediction

Portal dose prediction [2, 3, 4] can be used to verify if the planned treatment is similar to the actual treatment. If the predicted portal dose is the same as the measured portal dose, then the planned and the treatment situation are assumed to be the same. However, if there is a deviation between measured and predicted portal dose, then it is not always clear how this affects the dose deposited in the patient. One can see a difference but cannot tell if this difference is of importance, or how the dose distribution in the patient has changed. With this method it is possible to show so-called 'Organ Motion', the day-to-day internal movement of organs relative to bony structures, due to f.e. gas pockets in the rectum [5].

Exit plane reconstruction

Exit plane reconstruction is a 2-D reconstruction of the dose exiting the patient. Boellaard et al [6, 7] estimated the exit dose with a phantom study and were able to predict this exit dose for homogeneous and inhomogeneous phantoms with an accuracy of 2% and 2.5%, respectively. No clinical data were presented for this method. Bogaerts et al [8] found that if the portal image was taken close to the patient (i.e. air gap of 5 cm), then the portal dose has to be corrected for beam divergence only to estimate the exit dose. If the portal dose profile was taken with a 30 cm air gap between patient and detector, no correction had to be applied. In this case, the accuracy is within 3% of the exit profile. For other distances, f.e. 20 cm air gap the error increases up to 15%.

Midplane reconstruction

The first experimentally verified midplane reconstruction algorithm [9] used portal films in combination with diodes to measure the entrance and the exit dose. The calculated midplane doses were within 3% compared to ionization chamber measurements. Boellaard et al. [10] estimated the midplane dose with a physical model that was an extension of the earlier derived exit dose reconstruction. By applying a physical model (i.e. a correction for divergence, attenuation and patient scatter at the midplane) this reconstruction was able to achieve an accuracy of 3%. This method was only suitable if the phantom was midplane symmetric, deviations from this ideal geometry lead to larger differences up to 8%. By using this method for larynx, prostate and breast treatments, deviations smaller than 2.5% were found, but for the treatment of lung cancer the differences were large and up to 10% [11].

1.3 Three-dimensional dose reconstruction

3-D Dose reconstruction can be done with back projection methods [12, 13], using the dose information in the portal plane to obtain the dose in the patient. In a way, the method is similar to the forward treatment planning process. However, there are a few extra steps necessary if this method is compared to the treatment planning. These steps are discussed below.

Separation of scatter and primary dose/fluence

A portal dose image is taken during treatment of the patient. This 2-D dose image consists of a primary part and a patient scatter part. The primary part is related to the radiological thickness along the ray line from the point of detection to the source of the linear accelerator. The scattered part can not be related to the specific ray line or point in the patient because it comes from every

point inside the patient. Thus the first step for the back projection algorithm is the extraction of the 2-D primary dose distribution, more specific the primary fluence $\phi(E, \mathbf{r})$, with E the energy of the photon fluence and $\mathbf{r}$ the coordinate in the portal plane .

Back projection of primary fluence

The second step is the back projection of the primary dose through the patient. The patient is represented as a 3-D matrix with electron densities $\rho(\mathbf{s})$, f.e. obtained by a CT scan. The primary fluence in the patient $\Phi(E, \mathbf{s})$ can be calculated at every point inside this matrix by correcting the primary portal fluence $\phi(E, \mathbf{r})$ for beam divergence and attenuation,

$$\Phi(E, \mathbf{s}) = \tag{1.1}$$

$$\phi(E, \mathbf{r}) \left(\frac{\mathrm{SDD} + |\mathbf{r}|}{|\mathbf{s}|} \right)^2 \exp\left(+ \int_l \mu(E, \mathbf{s}) dl \right),$$

with the integral taken along the ray line l from portal image point $\mathbf{r}$ in the direction of the source to the reconstruction point $\mathbf{s}$, $\mu(E, \mathbf{s})$ is the corresponding attenuation coefficient and SDD is the distance from the source to the portal plane.

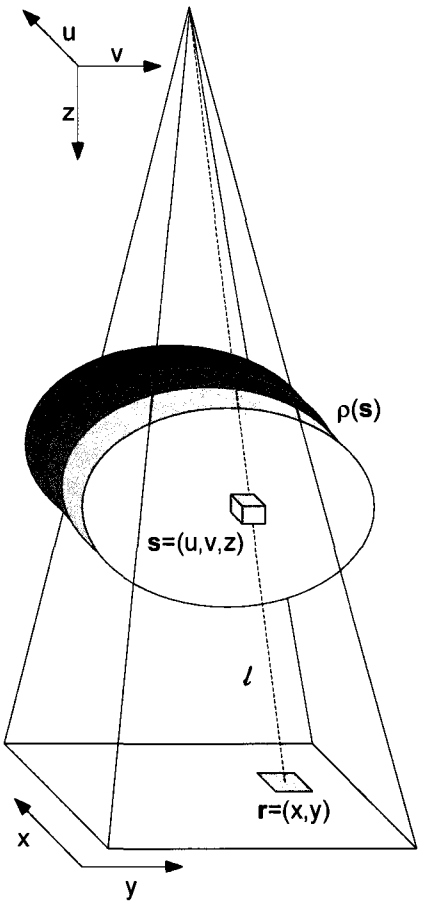

Figure 1.1: Schematic view of the back projection process. The patient is represented in the $\mathbf{s} = (u, v, z)$ coordinate system with the origin located at source. The portal image is a plane $\mathbf{r} = (x, y)$ in the coordinate system $\mathbf{s}$ with a fixed z-coordinate.

Calculation of Patient Dose

Once the primary fluence distribution inside the patient is known, this fluence is converted to another quantity $T(E, \mathbf{s})$, the total energy released per unit mass (TERMA):

$$T(E, \mathbf{s}) = E \frac{\mu(E, \mathbf{s})}{\rho(\mathbf{s})} \Phi(E, \mathbf{s}). \tag{1.2}$$

Then the conversion from TERMA to patient dose $D(\mathbf{s})$ can be made with so-called convolution kernels[2] $h(E, \mathbf{s})$. This step is similar to the way dose can be calculated with a treatment planning system:

$$D(\mathbf{s}) = \int_E \iiint_{\mathbf{s}'} T(E, \mathbf{s}') h(E, \mathbf{s} - \mathbf{s}')) d^3 s' dE. \tag{1.3}$$

As shown in eq. (1.3) each energy component has to be calculated individually, however one can also approximate this integral by taking only one energy component of the radiation, the average energy.

If the dose is measured in the portal image $D^P(\mathbf{r})$ instead of the fluence $\phi(E, \mathbf{r})$ then an approximated but simplified version of the back projection is possible [14]. The back projection step is the same as in eq. (1.1) but without the energy dependence, resulting in a primary dose distribution $D^P(\mathbf{s})$. The step of the TERMA calculation can be skipped, and the final calculation of the patient dose $D(\mathbf{s})$ can be estimated as the summation of the primary dose $D^P(\mathbf{s})$ and a patient scatter dose $D^S(\mathbf{s})$:

$$D^S(\mathbf{s}) = \left(K^{patient}(\mathbf{s}) \cdot \mathrm{NSPR}(T) \right) \otimes D^P(\mathbf{s}), \tag{1.4}$$

[2]These kernels are usually calculated from Monte Carlo simulations; the convolutions method are exact for homogeneous objects but an approximation for objects with heterogeneities.

with $K^{patient}$ a scatter kernel[3] and NSPR(T) is the normalized-scatter-to-primary ratio [10], a constant depending on the transmission T and $\otimes$ denotes a convolution.

Compare reconstructed dose with planned dose

The final step is to compare the reconstructed dose with the dose from the treatment planning system. If the reconstructed dose is f.e. lower as the planned dose, an additional or adapted treatment fraction can be given. In this way, an independent verification of the planned dose is possible; possible errors in the delivery can be detected and the treatment can be adjusted if necessary.

In this report the first step of the 3-D dose reconstruction is investigated; a detailed description of the portal dose dependencies. The acquisition of the 3-D electron density matrix is the next important step for the dose reconstruction method. To make the dose reconstruction completely independent of the treatment planning process this step has to be a treatment-time CT-scan.

[3]Louwe et al [14] described this kernel as $K(r) = c_1 e^{-c_2 r}/r^{c_3}$, the constants are fitted to phantom measurements.

Chapter 2

The Physics of Radiotherapy

In this chapter, a framework of the physics involved in radiotherapy is discussed. For a detailed discussion about this subject see textbooks like Khan [15] or Metcalfe et al [16]. First, the attenuation of a photon beam is discussed in section 2.1, then the interaction processes of photons with matter in section 2.2. Also the physical properties and the generation of a clinical photon beam produced by a linear accelerator is discussed (section 2.3) as well as the measurement of dose behind a patient with an Electronic Portal Imaging Device (section 2.4).

2.1 Attenuation coefficient

A mono-energetic photon beam that passes through an attenuator deposits some of the energy in the medium. The physical interactions involved in this process are dependent on the energy of the photons. The photons that do not interact with the attenuator are called the primary photons. The photons that do interact are either absorbed in the medium or scattered in a new direction. The number of photons dN that is removed from the incident beam N (either absorption or scattering) depends on the thickness dx of the attenuator and a constant specific for the material, the attenuation coefficient μ (or linear attenuation coefficient [cm^{-1}] if x is expressed as a length [cm]):

$$dN = -\mu N dx. \tag{2.1}$$

This differential equation can be solved and the number of primary photons $N(x)$ that pass through an attenuator without interaction can be written as

$$N(x) = N_0 e^{-\mu x}, \tag{2.2}$$

with N_0 the number of incident photons. Because the attenuation coefficient is only a function of the energy of the photon and the atomic composition of the material, one can divide the coefficient μ by the density ρ of the material. This results in the mass attenuation coefficient μ/ρ. This constant is not a function of the density but only depends on the photon energy and atomic structure of the attenuator.

A clinical photon beam is not mono-energetic but consists of a spectrum of energies. The attenuation of the clinical photon beam will differ from the ideal exponential decay. The mean energy of the spectrum of the photon beam will shift towards a higher energy for increasing attenuator thicknesses which results in a decrease in attenuation. This phenomenon is called *beam-hardening*.

2.2 Interaction of x-rays with matter

The interaction of photons with matter depends on the energy of the photons. For radiotherapy photon energies (4 MeV – 10 MeV) there a three main interaction processes[1]: the photoelectric effect, Compton scattering and pair production. The total attenuation coefficient μ/ρ is the sum of the individual processes:

$$\mu/\rho = \tau/\rho + \sigma_c/\rho + \pi/\rho, \tag{2.3}$$

with τ, σ_c and π the attenuation coefficients for photoelectric effect, Compton scattering and pair production, respectively. The individual processes will be discussed.

2.2.1 Photoelectric effect

The photoelectric effect occurs when a photon interacts with an atom and ejects one of the orbital electrons from the atom. The photon is completely absorbed and one electron is ejected from the K, L or M shell. The energy of the ejected electron is equal to the energy of the photon E minus the binding energy of the electron. The vacancy in the shell where the electron is ejected can be filled by an electron from the outer shells with the emission of a characteristic x-ray, or by the emission of so-called Auger electrons. The probability of photoelectric effect depends on the photon energy and the atomic number of the material Z:

$$\tau/\rho \propto Z^3/E^3. \tag{2.4}$$

The photoelectric effect is the most important process for radiology.

2.2.2 Compton scattering

The most important photon interaction process for therapeutic beam energies is Compton scattering. From 200 keV to 2 MeV this is in fact the only important process for soft tissues. Compton scattering occurs when a photon with energy E interacts with a free electron in the outer shell of the atom and this electron is ejected with an energy E_k. The energy of the photon after interaction (i.e. scattered photon) E' is equal to $E - E_k$. Since momentum is also conserved for this elastic scattering, the three energies are related to each other by:

$$E_k = E\left(\frac{\alpha(1-\cos\theta)}{1+\alpha(1-\cos\theta)}\right), \tag{2.5}$$

$$E' = E\left(\frac{1}{1+\alpha(1-\cos\theta)}\right), \tag{2.6}$$

with $\alpha = E/m_0c^2$, the ratio of the incident photon energy to the electron rest mass energy (0.511 MeV), and θ the angle between the scattered photon direction and the incident photon direction.

Compton differential cross section

The differential cross section per electron $d\sigma_e/d\Omega$ for Compton scattering was derived by a quantum mechanical analysis by Klein and Nishina:

$$\frac{d\sigma_e}{d\Omega} = \frac{d\sigma_0}{d\Omega}F_{KN}. \tag{2.7}$$

[1]Actually there are five: also coherent scattering and photo-desintegration. For coherent scattering there is no energy transferred to the medium, only the direction of the incident photon is changed. This phenomenon is only important for energies below 10 keV or high Z-materials. For very high photon energies (above 10 MeV) photo-desintegration can occur; a reaction between the photon and the nucleus.

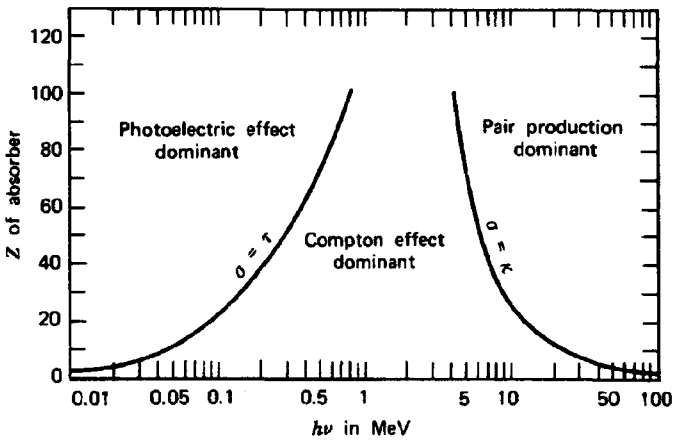

Figure 2.1: Relative importance of the three photon interaction processes[17].

The term $d\sigma_0/d\Omega$ is the classical scattering expression and F_{KN} is the Klein-Nishina factor:

$$\frac{d\sigma_0}{d\Omega} = \frac{r_0^2}{2}\left(1+\cos^2\theta\right), \tag{2.8}$$

$$F_{KN} = \left(\frac{1}{1+\alpha(1-\cos\theta)}\right)^2\left(1+\frac{\alpha^2(1-\cos\theta)^2}{(1+\alpha(1-\cos\theta))\,(1+\cos^2\theta)}\right), \tag{2.9}$$

with r_0 the classical electron radius.

Because Compton scattering is an interaction with the outer electron of the atom, it is independent of the atomic number Z and only depends on the number of electrons per gram. Except for hydrogen, this number is approximately constant over a wide range of atomic numbers. The Compton scattering also slightly decreases with photon energy, which can be described by [16]:

$$\sigma_c/\rho \propto E^{-1/2}. \tag{2.10}$$

2.2.3 Pair production

If the photon passes close enough to the nucleus, then the photon can interact with the electromagnetic field of the nucleus and a positron and an electron can be produced. This interaction process is called pair production. Pair production can only occur when the energy of the photon E is greater than $2m_0c^2 = 1.022$ MeV, the rest mass energy of a positron and an electron. The remaining energy of the photon ($E - 1.022$ MeV) is spread over the positron and the electron as kinetic energy. The positron travels through the medium in a same way as the electron until it interacts with another free electron; both the electron and positron disappear and 2 photons of 0.511 MeV are emitted in opposite direction, this radiation is called annihilation radiation.

Above the threshold energy of 1.022 MeV, the probability of pair production logarithmical increases with the energy and proportional with the atomic number Z,

$$\tau/\rho \propto Z \log E. \tag{2.11}$$

The relative dependence of the three photon interaction processes as a function of atomic number and photon energy is graphically shown in figure 2.1.

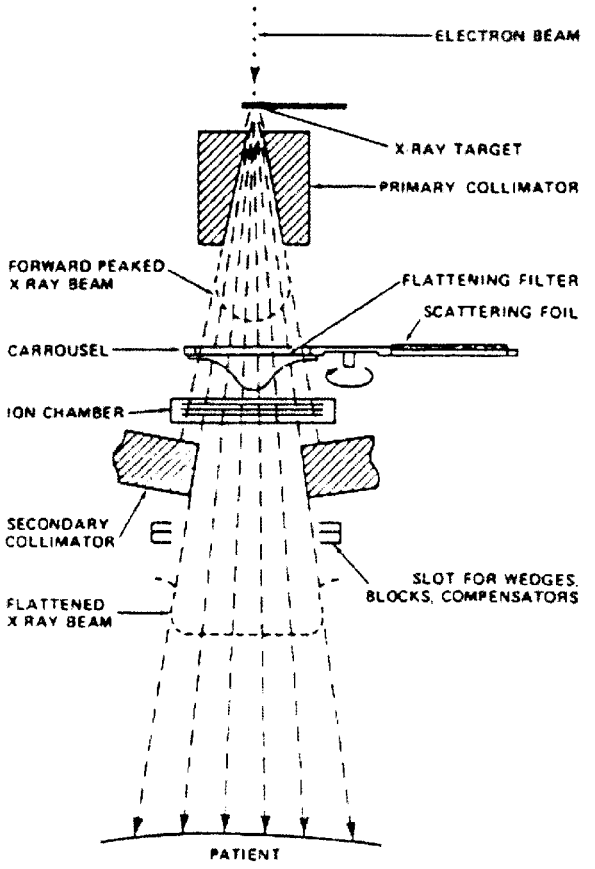

Figure 2.2: Schematic drawing of the treatment head of a linear accelerator; picture taken from Khan [15].

2.3 Photon beam generation with a linear accelerator

A linear electron accelerator (linac) is the most frequently used machine to produce clinical radiation, both electrons and photons can be produced with a linac. The linac currently used at MAASTRO CLINIC is the Elekta SL15. In figure 2.2, a schematic overview is given of the treatment head of a linac and the generation of a clinical photon beam is described below.

The first part of a linac (not shown in figure 2.2) is the same for both the generation of an electron as well as a photon beam. First the electrons are generated by an electron gun and ejected into an accelerator tube. Inside this tube the electrons are accelerated by a travelling or standing electromagnetic wave with a frequency around 3 GHz. This travelling or standing wave can be produced by a magnetron or klystron. The electrons are accelerated from an initial low energy of around 50 keV to the high energy region (up to 30 MeV). At the end of the accelerator tube usually a bending magnet is placed to direct the beam towards the patient.

The second part of the machine (shown in figure 2.2) is different for the production of an electron or a photon beam. In the case of a photon beam (x-rays), the narrow electron beam exiting from the accelerator tube hits a so-called x-ray target. This target is made of a high Z material. In this target so-called 'bremsstrahlung' is produced because a high energetic electron passes the nucleus of the target at a close distance and the energy of the electron is converted in a spectrum of x-ray energies; the maximum energy is equal to the maximum incident electron

energy. The average energy is approximately one third of this maximum energy[2] [15]. The x-rays then pass the primary collimator. Because the production of the x-rays is forwardly peaked an additional filter is inserted in the beam, the flattening filter. This filter makes the intensity of the x-ray beam uniform across the entire field.

The photon beam then passes through the ionization chamber. This dose monitoring instrument measures the dose rate and the integrated dose. It controls the actual amount of dose delivered to the patient.

The photon beam is then blocked by the secondary collimator to create the specific field size. For Elekta linacs, this collimator consists of two pairs of jaws that block the beam. These jaws can be moved independently from each other to create field sizes from 0×0 to 40×40 cm^2 at a distance from the target of 100 cm. These field sizes can be square or rectangular. Because the jaws can be moved independently from each other, also asymmetric fields can be created. In asymmetric fields the center of the collimator axis does not coincide with the center of the field.

The treatment head is fixed to the gantry and can be rotated over 360 degrees. The point where the center of the gantry rotation intersects with the center of the collimator axis is called the *isocenter*; this distance is fixed at 100 cm from the target.

2.4 Electronic Portal Imaging Device

An Electronic Portal Imaging Device (EPID) used for radiotherapy is a device that is able to make digital pictures of high energetic x-ray radiation. In figure 2.4 a schematic view of the device is shown as it is used in clinical setting.

There are several commercially available EPIDs. Currently at MAASTRO CLINIC, a so-called video-based EPID is used; the Theraview-NT EPID (Cablon Medical, the Netherlands). Only this EPID will be discussed here. For a detailed overview of other types of EPIDs see the review article of Boyer et al [18].

The video-based EPID is mounted on the gantry at a distance to the target that can usually vary from 140 to 160 cm. The high-energetic photons hit upon a metal detector plate which can release high-energetic electrons. The metal plate is coated with a fluorescent screen of Gd_2O_2S. The high-energetic electrons release visible photons in the fluorescent screen and these visible photons are reflected through an optical system of mirrors to a camera. The camera signal can be digitally read out and can be further processed (see figure 2.3).

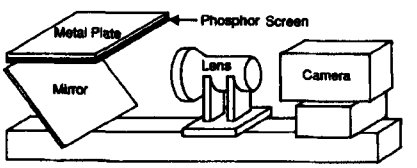

Figure 2.3: Schematic view of the video-based EPID [18].

The images acquired during treatment can be used to check patient positioning because the bony structures attenuate the photon beam more than the surrounding tissue and the signal at the EPID is thus lower in these regions. These portal images can be compared with the images made from either simulation photos or with digitally reconstructed radiographs (DRR) from the treatment planning system.

The images can also be converted from intensity (grayscale) images to dose images. This offers the possibility for quality control and in-vivo dosimetry as described in chapter 1. A dosimetric calibration procedure for CCD-based EPIDs is described by Heijmen et al [19], which is accurate up to 1% at the beam axis and the accuracy slightly decreases off-axis up to 4.5% for highly asymmetric and wedged fields [20, 21, 22].

[2]The x-ray beam is heterogeneous in energy and designated by megavolts as if it was created by applying this voltage across an x-ray tube.

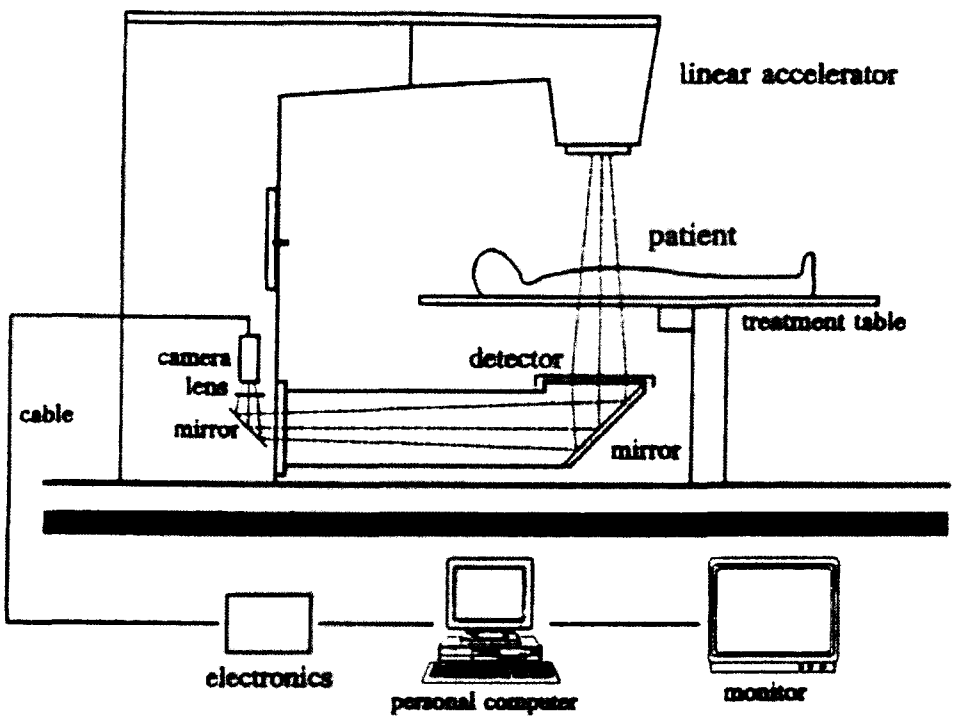

Figure 2.4: Schematic drawing of a video-based EPID at a linear accelerator; picture taken from Althof et al [23].

Chapter 3

Portal Dose Images

Portal dose images are dose distributions at a plane distal to the patient. These images can be acquired either by exposing a film or with electronic portal imaging devices (EPID). The dose distribution $I(\mathbf{r},t)$ at position $\mathbf{r}$ in the portal image behind an object with radiological thickness distribution t can be described as the summation of a primary part $P(\mathbf{r},t)$ and a patient scattered part $S(\mathbf{r},t)$:

$$I(\mathbf{r},t) = P(\mathbf{r},t) + S(\mathbf{r},t). \tag{3.1}$$

The primary dose is a function of the radiological thickness; the scattered dose is dependent on various factors which are described in section 3.1. The separation of the primary and the scattered part needed for the back projection as described in section 1.3 is not trivial. The scattered contribution can be as high as 25% for some configurations (e.g. large phantom thickness, large field area, small air gap) [24]. To estimate the scattered part, various methods have been presented in literature. An overview of most of these methods is given in section 3.2. A comparison between the methods is made in section 3.3 and the (dis)advantages of each method are discussed.

3.1 Portal dose dependencies

Measuring dose

The golden standard for dose measurements in radiotherapy is an ionization chamber in a watertank. Dose measurements can be performed in different media like water, air or PMMA. In this report, all measurements are performed under full scatter conditions, i.e. measurements are performed in a watertank. The next sections describes the various factors that influence the dose in the portal image in detail.

Primary dose

The primary dose $P(\mathbf{r},t)$ is only a function of the radiological thickness t of the attenuator (i.e. phantom or patient) and the effective attenuation coefficient $\mu(r,t)$, following eq. (2.2):

$$P(\mathbf{r},t) = O(\mathbf{r})e^{-\mu(r,t)\cdot t}, \tag{3.2}$$

with $O(\mathbf{r})$ the dose distribution without the attenuator in the beam. The effective attenuation coefficient depends on the atomic structure of the phantom in the beam and the energy of the incident photon. In this report only 6 MV x-rays are analysed. For higher x-ray energies (e.g. 10 MV x-rays) the attenuation coefficient generally decreases and the amount of primary dose is thus higher than for the 6 MV x-rays. Because a clinical photon beam is poly-energetic and the spectrum also changes with off-axis locations, this attenuation coefficient depends on the thickness t and off-axis distance $r = |\mathbf{r}|$.

Scattered dose

The scattered dose $S(\mathbf{r}, t)$ in a portal image depends on more factors than the primary dose. An overview of the various factors is shown in table 3.1 and described below. The physics describing the scatter phenomena is described in section 2.2.

Number of monitor units[1]. Because the dose depends linearly on the number of monitor units, this property is not so interesting for the dose in portal images. In fact, to eliminate the effect of fluctuations in the output of the linear accelerator to dose measurements, the transmission is measured.

X-ray energy. The energy of the x-rays used in this report is 6 MV. The underlying physics of the scattering processes does not significantly alter if this energy is changed to 10 MV, see section 2.2. The attenuation coefficient μ will decrease resulting in a higher primary dose and a lower scattered dose if the photon energy is increased from 6 to 10 MV.

Wedge. The presence of a wedge needs a little more explanation, this due to the fact that there are two methods to create a wedge. A static wedge a slab of material (lead or steel) which can be inserted into the beam; the static wedge produces a shift in the beam spectrum towards higher energies for the thicker side of the wedge due to beam hardening which has to be taken into account by a slightly different attenuation coefficient [25]. A dynamic wedge is produced by closing the collimator jaws during irradiation, in this case the attenuation coefficient does not change. The influence of a wedge to the scattered dose is not investigated in this report.

Field size. Another important factor influencing the dose distribution in portal images is the shape and the size of the field. In general, the scattered transmission increases with larger field areas but the two-dimensional distribution is highly non-constant. The scattered dose is created not only by the primary beam but also by the scattered photons. This makes the scatter distribution different for each field size. The effects of square and rectangular as well as symmetric and asymmetric field sizes are investigated. Irregular field sizes, created by either a multi leaf collimator (MLC) or blocks are not investigated.

Type of object in the beam. The type of object placed in the beam is the most important factor influencing the scattered dose distribution. The phantoms are arranged in three groups. First, based on the phantom material; homogeneous or inhomogeneous. Second, based on the placement of the phantom relative to detector or isocenter. Third, based on the symmetry of the phantom around its geometrical midplane.

3.2 Separation of primary and scattered dose in portal dose images

In this section various methods are discussed for the calculation or measurement of the primary and scattered dose in portal images.

3.2.1 Large air gap

Boellaard et al [6] estimated the primary component by taking EPID images with a large air gap between EPID and phantom (i.e. 90 cm). At large air gaps, the scatter that reaches the portal image is assumed to be small and constant over the dimensions of the EPID.

The primary dose $P(\mathbf{r}, t)$ can also be estimated by extrapolating the measured transmission values to a field size of 0×0 cm^2; then the scattered dose $S(\mathbf{r}, t)$ for the other field areas is calculated by subtracting this extrapolated primary dose $P(\mathbf{r}, t)$ from the total image. For other air gaps, the primary distribution is simply calculated by taking the primary distribution at this large air gap and applying the inverse square law $ISQL$. The scattered contribution is then calculated using:

$$S(\mathbf{r}, t) = I(\mathbf{r}, t) - (P(\mathbf{r}, t) \cdot ISQL). \tag{3.3}$$

[1]The number of monitor units (MU) is the common standard in radiotherapy to describe the amount of dose delivered. The definition is that 1 MU delivers 1 cGy at reference conditions.

Table 3.1: Factors influencing the dose in portal images; the italic printed factors are analysed in this report.

Linear Accelerator	
Number of Monitor Units	Adjustable
Energy of x-rays	*6 MV* or 10 MV
Wedge in the beam	*No* / Static / Dynamic
Field area[1]	*3×3 - 24×24 cm²*
Field shape	*square* / *rectangular* / irregular
	symmetric / *asymmetric*
Phantom	
Material	*Homogeneous* / *Inhomogeneous*
Isocenter symmetric	*Yes* / *No*
Midplane symmetric	*Yes* / *No*
Detector	
Measurement conditions	Full scatter water phantom
Detector type	Ionization chamber
Detector depth	2.5 cm
Source Surface Distance	147.5 cm
Source Detector Distance	150 cm

[1]The largest field area used is a 24×24 cm² field; this because of the maximum width of phantom material of 30×30 cm².

3.2.2 Primary dose by ray tracing

By making use of the attenuation map (e.g. CT data), one can calculate the primary distribution exiting from the phantom. If the incident beam profile $O(\mathbf{r})$ and this attenuation map are known, then it is possible to calculate the primary transmission $P(\mathbf{r}, t)$:

$$P(\mathbf{r}, t) = O(\mathbf{r}) \cdot e^{-\mu(r,t)t}, \tag{3.4}$$

with t the radiological thickness of the phantom and $\mu(r, t)$ the attenuation coefficient of the phantom at the calculated point. The scattered part S can then be estimated by subtracting this primary part P from the measured portal image I.

3.2.3 Monte Carlo

Monte Carlo simulations can track what happens to the incident photon beam when it interacts with matter. It is thus possible to follow the photon through the phantom/patient. It is also possible to calculate a dose distribution in a plane after the beam has interacted with the patient. The great advantage of Monte Carlo techniques is that a separation can be made between the photons which have interacted with the phantom/patient (the scattered part) and photons which have not interacted at all (the primary part).

3.2.4 Superposition with pencil beam scatter kernels

The scatter contribution can be calculated from phantom properties (thickness, attenuation coefficient, etc.) by a superposition of the open beam fluence with so-called pencil beam scatter kernels (PBSKs). These scatter kernels can be calculated either from Monte Carlo simulations

[26], analytically calculated kernels by evaluating Compton and pair productions cross sections [27, 2] or empirically derived kernels from measurements [3].

The scatter kernels $K(t,r)$ are calculated for a known thickness t by evaluating so-called 'pencil beams'; the scatter in a plane distal to the phantom is calculated from these small narrow beams. The scattered radiation for a beam area A is then calculated by a superposition of this open beam $O(\mathbf{r})$ with the pencil beam scatter kernels:

$$S(\mathbf{r},t) = \iint_{\mathbf{r}'\epsilon A} O(\mathbf{r}') \cdot K(t, \mathbf{r}-\mathbf{r}') d^2r'. \tag{3.5}$$

The problem with this algorithm is obtaining a good set of kernels and the phantom/patient thicknesses have to be known for the prediction of the scattered dose.

Iterative reconstruction of radiological thickness.
Hansen et al [26] have used these pre-calculated scatter kernels for the derivation of the primary dose and avoiding the need of phantom/patient information by calculating the primary dose and the radiological thickness with an iterative method:

1. Initial guess of $P(\mathbf{r},t) = I(\mathbf{r},t)$ and start iteration with n=1,
2. Radiological phantom thickness t^n can be calculated from $P^n(\mathbf{r},t) = O(\mathbf{r}) \cdot \exp\left[-\mu\,(r,t) \cdot t^n\right]$,
3. Choose the kernel $K(t^n, r)$ on the basis of t^n,
4. Scatter distribution calculation $S^n(\mathbf{r},t) = \iint_{\mathbf{r}'\epsilon A} O(\mathbf{r}') \cdot K(t^n, |\mathbf{r}-\mathbf{r}'|) d^2r'$,
5. Extraction of primary distribution $P^{n+1}(\mathbf{r},t) = I(\mathbf{r},t) - S^n(\mathbf{r},t)$,
6. Repeat steps 2-5 until the solution converges.

In this way an estimate is made of the radiological thickness, the primary and the scattered dose solely on the basis of the open beam image, the (transmission) portal image and the set of PBSKs.

3.2.5 Method Swindell & Evans

Swindell & Evans [28] have used Monte Carlo simulations to derive a simple physical model for the estimation of scatter for the *on-axis* transmission of homogeneous phantoms. The derived scatter-to-primary ratio $SPR = S/P$ is:

$$SPR = k_0 A t (1 + k_1 t)(1 + k_2 A), \tag{3.6}$$

$$k_0 = 0.0266 \left(\frac{L_1 + L_2}{L_1 L_2}\right)^2, \tag{3.7}$$

$$k_1 \cong 2 \cdot 10^{-3} \mathrm{cm}^{-1} \quad \text{for} \quad 60 \leq L_2 \leq 100\mathrm{cm}, \tag{3.8}$$

$$k_2 = -\frac{1}{2\pi}\left(\frac{1}{L_1^2} + \frac{1}{L_2^2} + \left(\frac{1}{L_1} + \frac{1}{L_2}\right)^2 \left(\frac{2}{3} + \frac{3\kappa}{2}\right)\right), \tag{3.9}$$

$$\tag{3.10}$$

with L_1 and L_2 the distance to the isocenter and the distance from isocenter to portal image respectively, and κ the mean energy of the beam. This physical model would be correct within 0.5% for thicknesses from 0–40 cm and (circular) beam areas up to 320 cm^2. This however is only an approximation of the on-axis scatter for homogeneous phantoms.

3.2.6 Constant scatter

The scattered part can also be estimated to be a constant, this is true if the EPID is at a large distance from the phantom and probably only holds if the phantom is not heterogenous [6].

3.2.7 Average scatter

If the scatter $S(\mathbf{r},t)$ for a set of configurations is known then the average scatter for the set of configurations can be calculated by averaging the N portal images to an averaged scatter image $\overline{S(\mathbf{r},t)}$:

$$\overline{S(\mathbf{r},t)} = \frac{1}{N}\sum_{i=1}^{N} S_i(\mathbf{r},t). \tag{3.11}$$

This averaged scatter can in the future be used as an estimation of the scatter.

3.3 Comparison of the methods

If a high degree of accuracy with an error of only a few percent of the total dose has to be achieved then the 'constant' and 'average scatter' method are not possible due to the high non-constant behavior of the scatter. The method proposed by Swindell & Evans is only correct for homogeneous phantoms and is only an estimate of the (0-D) on-axis scatter, hence not suitable for a 2-D estimation of the scatter. The methods that can be derived from measurements and not need complex Monte Carlo simulations are the 'Large Air Gap', 'Ray Tracing' and the 'Pencil Beam Scatter Kernels' methods.

Monte Carlo.
The Monte Carlo method is widely used as 'Golden Standard' to verify the actual dose deposition in inhomogeneous media. At MAASTRO CLINIC, a Monte Carlo code (XVMC, University of Tübingen, Germany [29]) is available but with this code it is not (yet) possible to make a difference between scattered and primary dose and this method is not further taken into account.

Large air gap.
The 'large air gap' method is not possible for the EPID used in MAASTRO CLINIC because the distance of the EPID from the source can only be varied from 140 to 160 cm and for this method the EPID has to be at large distance (e.g. 190 cm) from the source. A possible drawback is the small field of view at the isocenter due to the finite size of the EPID (e.g. 40 cm at 190cm from the source represents a field of view of $40 \cdot 100/190 = 21.1$ cm at the isocenter).

Ray tracing.
The drawback of the 'ray tracing' method is that this method can only be used if an attenuation map (CT-scan) is available. For the verification of the treatment process, it is preferred to use as less information in advance which makes the verification as independent as possible. The method only predicts the primary component and gives no information about the scattered dose distribution directly.

Pencil beam scatter kernels.
With the 'pencil beam scatter kernel' method, it is possible to predict the portal dose images within a few percent error [4]. An advantage is that the input data (the images with and without phantom/patient) are already routinely acquired per patient at MAASTRO CLINIC. Another advantage is that the model is able to extract the primary dose from the portal image. This is one of the input parameters for the three-dimensional dose reconstruction as described in section 1.3.

Based on the considerations mentioned above, the method chosen to describe the dose distribution in the portal image and is able extract the primary dose is the method based on the pencil beam scatter kernels. In this report the derivation of the PBSKs from measurements is discussed and not a derivation based on simulations by a Monte Carlo code as frequently is done in literature [30]. The method presented calculates the kernels from a set of transmission measurements on the beam axis from various field areas and phantom thicknesses.

Chapter 4

Portal Dose Prediction Model

Based on the considerations mentioned in chapter 3, a new model to predict the dose in portal images is developed. The definitions used in this report are given first (section 4.1), then some concepts are described on which the model is based. The use of pencil beam scatter kernels (section 4.2) and the use of a so-called equivalent homogeneous phantom concept (section 4.3) is explained. In section 4.4 the new model is presented, assumptions and approximations are discussed. Finally in section 4.5, some other possible applications of the model are briefly discussed. The measurement set-up and the accuracy of the model are discussed in chapter 5 and 6, respectively. The verification of the new model is performed using homogeneous and inhomogeneous phantoms. Also a clinical example of the treatment of breast cancer is presented.

4.1 Definitions

The dose distribution in a portal image at a distance $\mathbf{r} = (x, y)$ from the beam axis without an attenuator in the beam (i.e. phantom or patient) is called the open dose distribution $O(\mathbf{r})$, and $I(\mathbf{r}, t)$ is the dose distribution with a phantom or a patient with thickness t in the beam. The latter dose distribution is the summation of a primary dose $P(\mathbf{r}, t)$ and a scattered dose $S(\mathbf{r}, t)$:

$$I(\mathbf{r}, t) = P(\mathbf{r}, t) + S(\mathbf{r}, t). \tag{4.1}$$

From these quantities the total $T(\mathbf{r}, t)$, primary $T^P(\mathbf{r}, t)$ and scattered $T^S(\mathbf{r}, t)$ transmissions can be calculated:

$$T(\mathbf{r}, t) = \frac{I(\mathbf{r}, t)}{O(\mathbf{r})}, \qquad T^P(\mathbf{r}, t) = \frac{P(\mathbf{r}, t)}{O(\mathbf{r})}, \qquad T^S(\mathbf{r}, t) = \frac{S(\mathbf{r}, t)}{O(\mathbf{r})}. \tag{4.2}$$

4.2 Pencil beam concept

The pencil beam concept was originally developed for the calculation of dose inside the patient, see for example Ahnesjo et al [31]. The incident beam profile can be described as a superposition of many small pencil beams. It is assumed that the profile has the same properties over the area of the beam which is substituted with the pencil beams. The deposited dose inside a medium due to such a pencil beam is calculated from f.e. Monte Carlo simulations. The total dose is then calculated from the superposition of the pencil beams that describe the field.

For the prediction of dose in a portal image a similar concept is used. A schematic overview of the pencil beam concept is shown in figure 4.1. An infinitely thin pencil beam incidents on a phantom with known thickness t. Some photons do not interact with the phantom at all and exit the phantom (the primary photons). The photons that do interact are absorbed or change

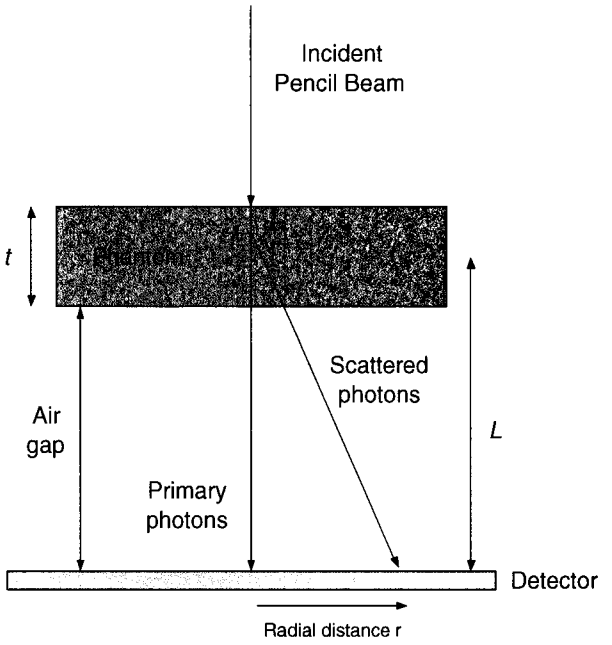

Figure 4.1: Schematic view of the pencil beam concept. A pencil beam incidents upon a phantom. Some photons do not interact (primary photons) and some photons have interacted and exit the phantom with a different angle (scattered photons).

direction and are detected at an off-axis location $r = |\mathbf{r}|$; the photons that have a changed direction are the scattered photons.

The function describing the spread of scattered photons at the off-axis locations is called the pencil beam scatter kernel. For a given beam spectrum and a homogeneous phantom placed symmetrically around the midplane, the kernel $K_L(t, r)$ is a function of the phantom thickness t and the distance L between detector and midplane of the phantom.

4.3 Equivalent homogeneous phantom concept

The equivalent homogeneous phantom (EHP) concept is introduced by Pasma et al [3]. Using this concept, an inhomogeneous phantom or patient is replaced with a homogeneous phantom taking into account the radiological path length and the center-of-mass. The EHP consists of two 2-D arrays. These two arrays are calculated by ray-tracing the photons from the source through the phantom to the detector. The matrix elements of the first array consist of the radiological thickness and the second array describes the coordinates of the center of mass, both taking into account the beam divergence[1]. The EHP can be derived by ray tracing through a CT-scan. See also figure 4.2 for a visual explanation of the concept.

4.4 Portal dose prediction model

Following the pencil beam and the EHP concept, the primary and the scattered dose can be calculated if the thickness of the attenuator and the open beam dose distribution is known. The calculation of the primary dose and the scattered dose distribution are done separate and the two distributions are summed to yield the total dose distribution.

[1]Conceptually it is the same as a digitally reconstructed radiograph (DRR) but with information about the center-of-mass and using the attenuation coefficients for MV x-rays instead of kV x-rays.

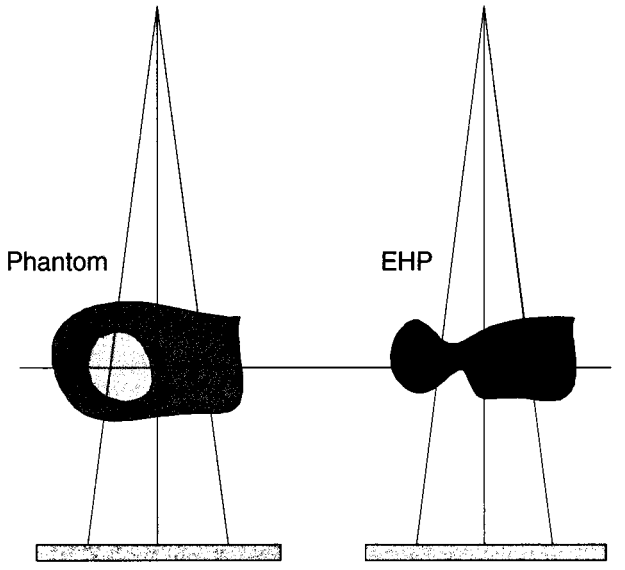

Figure 4.2: Visualization of the EHP concept. On the left the actual electron density is presented as a gray scale image and on the right the corresponding EHP is shown.

4.4.1 Prediction of primary dose

The effective attenuation is derived as a function of the phantom thickness t and the off-axis location r because a clinical photon beam is poly-energetic. In general, beam hardening[2] will occur with larger phantom thicknesses as a result of the shift in energy spectrum. Beam softening[3] is expected for off-axis locations due to off-axis differences in beam quality produced by the shape of the flattening filter.

The total primary dose can be calculated, following eq. (2.2), at each position by taking into account the attenuation coefficient $\mu(r,t)$ and the radiological thickness t (derived from the EHP):

$$P(\mathbf{r},t) = O(\mathbf{r})e^{-\mu(r,t)\cdot t}. \tag{4.3}$$

4.4.2 Prediction of scattered dose

The model to predict scattered dose in portal images is a combination of the pencil beam concept and the EHP concept. The physical interpretation of the scattered dose calculation is that it originates from the center-of-mass of the phantom. The total scatter produced by the column of phantom material can be replaced by a corresponding radiological thickness distributed symmetrically around the center-of-mass of the replaced column of phantom material, see figure 4.2. The scattered dose can then be calculated by applying the pencil beam model in relation with the EHP concept. The pencil beam scatter kernel describes the scattered portal dose for a particular ray line. The pencil beam scatter kernel for every ray line (pencil beam) is chosen on the basis of the information in the EHP, i.e. the thickness t and the distance of the center of mass to detector L. Assuming midplane symmetry (i.e. fixed L), the total scattered dose $S(\mathbf{r},t)$ is the superposition of the open beam dose $O(\mathbf{r})$ with the pencil beam scatter kernel $K(t,r)$. The specific kernel chosen is based on the radiological thickness at the point $\mathbf{r}$ examined

$$S(\mathbf{r},t) = \iint O(\mathbf{r}')K(t,|\mathbf{r}'-\mathbf{r}|)d^2r'. \tag{4.4}$$

The integral is taken over the entire field area.

[2]Beam hardening: The decrease of the attenuation coefficient.
[3]Beam softening: The increase of the attenuation coefficient.

Kernel functions

To avoid the use of Monte Carlo simulations [26, 30] for the derivation of the pencil beam scatter kernels, a new method is developed to calculate these scatter kernels from measurements. Pasma et al [3] calculated the scatter kernels numerically from transmission measurements using square field areas and applied a correction for the non-circular beam area. These kernels are very noisy and show non-physical behavior near the beam axis. The derivation presented is based on measurements and assuming a kernel shape.

With the new method presented in this report, the pencil beam scatter kernels are derived by fitting on-axis transmission measurements to a predefined kernel function. The on-axis transmission $T(\mathbf{r}=0,t)$ for various square field areas A and homogeneous phantom thicknesses t are fitted to describe the following relation:

$$T(\mathbf{r}=0,t) = c_1(t) + \iint_{(x',y')\epsilon A} \frac{O(x',y')}{O(0,0)} K(t, \sqrt{x'^2+y'^2}) dx'dy'. \tag{4.5}$$

Note that this equation is similar to the sum of equations (4.3) and (4.4) divided by the open beam dose $O(\mathbf{r})$ for the coordinate $\mathbf{r}=(x,y)=(0,0)$. The quantities $T(\mathbf{r}=0,t)$, $O(\mathbf{r})$ and A are measured and the coefficient $c_1(t)$ and $K(t,r)$ are fitted; $c_1(t)$ is the primary transmission $T^P(\mathbf{r},t)$ and $K(t,r)$ is the pencil beam scatter kernel.

Various functions can be used to fit the scatter kernel function $K(t,r)$. Three functions are examined: a Gaussian profile, an isotropic point source model and a model based on the Klein-Nishina differential cross section.

Fit function 1: Gaussian profile

As an empirical approach, the first fitting function is a Gaussian shaped profile with coefficients $c_2(t)$ and $c_3(t)$

$$K(t,r) = c_3(t) e^{-c_2(t) r^2}, \tag{4.6}$$

with $r=\sqrt{x^2+y^2}$.

Fit function 2: Isotropic point source

The second fitting function is a (virtual) radially isotropic point source at a distance of $c_2(t)$ above the detector plane with strength $c_3(t)$

$$K(t,r) = \frac{c_3(t) c_2(t)}{\left(r^2 + c_2(t)^2\right)^{3/2}}, \tag{4.7}$$

with $r=\sqrt{x^2+y^2}$.

Fit function 3: Klein-Nishina differential cross section

The third fitting function is based on single scattered photons. These scattered photons can in principle be derived analytically by using the scattering cross section for Compton scattering. This function is known as the Klein-Nishina differential cross section, see eq. (2.8) and (2.9):

$$K(t,r) = \frac{c_2(t)}{2} \left(\frac{1}{1+\alpha(1-\cos\theta)} \right)^2 \left(1 + \cos^2\theta + \frac{\alpha^2(1-\cos\theta)^2}{1+\alpha(1-\cos\theta)} \right) \frac{\cos\theta}{r^2+z^2}, \tag{4.8}$$

with θ the scattered angle of the incident photon and α the ratio of the incident photon energy E to the electron rest mass energy $m_0c^2 = 0.511$ MeV,

$$\cos\theta = \frac{z}{\sqrt{r^2+z^2}}, \qquad \alpha = \frac{E}{m_0c^2}, \qquad r=\sqrt{x^2+y^2}.$$

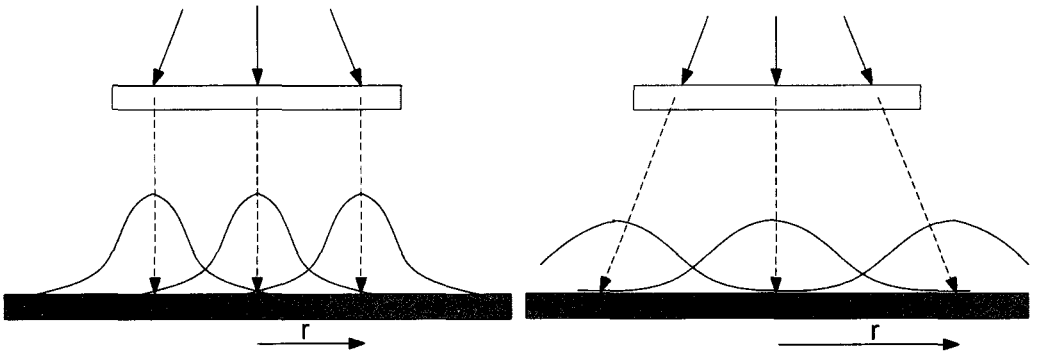

(a) Parallel approach (b) Tilted approach

Figure 4.3: Scatter estimation: Parallel approach versus the kernel tilting approach.

The factor $\cos\theta/\left(r^2+z^2\right)$ is used to convert from spherical coordinates to cartesian (plane) coordinates. Assuming that the scattered radiation comes from the center of the phantom (following the EHP concept) and that the detector is placed at a distance 150 cm from the source, then $z = 50$ cm and the mean energy of the polyenergetic 6 MV beam is assumed to be $\frac{1}{3}$ of the nominal energy [15], $E = 2$ MV.

Fitting geometry

For the concept of the EHP and the pencil beam two approaches are possible: a parallel beam approach and a kernel tilting approach. The two approaches differ in whether the divergence of the beam is taken into account for the calculation of the scatter contribution, or not. In figure 4.3, the two concepts are shown and a visual explanation for the difference is given.

The parallel approach does not take into account the divergence of the beam and simplifies the creation of the scatter as if it originate from the point of interaction of a parallel photon beam.

The kernel tilting approach does take into account the beam divergence. The scatter kernel is calculated as if scatter originates from a virtual point at a distance above the detected point parallel to the beam axis in the plane behind the phantom.

Fitting procedure

The fitting procedure is implemented as a minimization problem[4] in Matlab (version 6.5.1, The MathWorks, Inc.). The coefficients $c_1(t)$, $c_2(t)$ and $c_3(t)$ are fitted to yield the smallest absolute difference between measured and fitted on-axis transmissions. Another way of deriving the pencil beam scatter kernels in a semi-analytical way is described in appendix A; this method uses circular fields as incident beams and is not used in this report.

4.4.3 Overview of the prediction model

If the attenuation coefficient, the EHP and the pencil beam scatter kernels are known then portal dose distributions can be calculated. This procedure is listed below:

1. Calculate radiological thickness: t,
2. Calculate primary dose: $P(\mathbf{r},t) = O(\mathbf{r}) \cdot \exp\left[-\mu\left(r,t\right) \cdot t\right]$,
3. Calculate scattered dose: $S(\mathbf{r},t) = \iint O(\mathbf{r}')K(t,|\mathbf{r}-\mathbf{r}'|)d^2r'$,
4. Add primary and scatter: $I(\mathbf{r},t) = P(\mathbf{r},t) + S(\mathbf{r},t)$.

[4]The specific function is `fminsearch` that uses a simplex search method to minimize the difference between measured and fitted values/data.

4.5 Other applications of the model

The prediction model describes the relation between three parameters: (1) the open beam dose $O(\mathbf{r})$, (2) the portal dose $I(\mathbf{r},t)$ and (3) the radiological thickness t. If two parameters are known than the third can be calculated from the other two. However, this holds only for phantoms that are midplane symmetric. This limitation is necessary because the EHP concept is not only based on the radiological thickness but also on the distance if the center-of-mass to detector. For midplane symmetric phantoms, this distance is approximately constant over the EHP.

Model to extract the radiological thickness

The above described prediction model can also be used to calculate the radiological thickness which is related to the primary dose by the attenuation coefficient, eq. (4.3). The primary dose is the input for the three dimensional dose reconstruction algorithm, described in chapter 1. The extraction of the radiological thickness can be calculated in an iterative way as described by Hansen et al [26]. The iterative steps are described in section 3.2.4 but for completeness shown again below:

1. Initial guess of $P(\mathbf{r},t) = I(\mathbf{r},t)$ and start iteration with n=1,
2. Radiological phantom thickness t^n can be calculated from $t^n = \frac{1}{\mu(r,t)} \cdot \ln\left(\frac{P^n(\mathbf{r},t)}{O(\mathbf{r})}\right)$,
3. Choose the kernel $K(t^n,r)$ based on t^n,
4. Scatter distribution calculation $S^n(\mathbf{r},t) = \iint O(\mathbf{r}')K(t^n,|\mathbf{r}-\mathbf{r}'|)d^2r'$,
5. Extraction of primary distribution $P^{n+1}(\mathbf{r},t) = I(\mathbf{r},t) - S^n(\mathbf{r},t)$,
6. Repeat steps 2-5 until the solution converges.

Model to extract the incident beam profile

Analogous to the way the radiological thickness is extracted, also the open beam dose can be reconstructed. Input parameters for the reconstruction of incident beam profile are the portal dose $I(\mathbf{r})$ and the radiological thickness. If these two parameters are known, the third can be calculated using an iteration procedure:

1. Initial guess of $O(\mathbf{r}) = I(\mathbf{r},t) \cdot \exp\left[+\mu\,(r,t) \cdot t\right]$ and start iteration,
2. Choose the kernel $K(t,r)$ based on t,
3. Scatter distribution calculation $S^n(\mathbf{r},t) = \iint O^n(\mathbf{r}')K(t,|\mathbf{r}-\mathbf{r}'|)d^2r'$,
4. Extraction of primary distribution $P^n(\mathbf{r},t) = I(\mathbf{r},t) - S^n(\mathbf{r},t)$,
5. New estimate of open beam dose $O^{n+1}(\mathbf{r}) = P^n(\mathbf{r},t) \cdot \exp\left[+\mu\,(r,t) \cdot t\right]$
6. Repeat steps 2-5 until the solution converges.

Spies et al [32] have used this algorithm with Monte Carlo calculated scatter kernels for the extraction of the incident beam profile.

Chapter 5

Portal Dose Measurements

The measurements performed to assess the accuracy of the prediction model are divided into four main categories. The first category describes the derivation of the input parameters of the model; the attenuation coefficient and the pencil beam scatter kernels. The second categorie describes the accuracy of the various geometries and scatter kernels for homogeneous phantoms. The third category, the model is applied to predict the dose for inhomogeneous phantoms and phantom geometries that deviate from the fitting geometry. And as a final category, the model is tested on actual clinical data; the treatment of breast cancer. The numbering of the sections is the same as the sections with results shown in chapter 6. An overview of all the measurements is given in table 5.2 at the end of this chapter. All measurements are performed with a 6 MV clinical photon beam from an Elekta SL15 linear accelerator.

Point measurements

The measurements presented in this report are done with various measurement instruments. The type of detector is also chosen to match this golden standard; an ionization chamber (Scanditronix Wellhofer CC13) placed in a watertank (Scanditronix Wellhofer Blue Phantom). The depth of measurement is chosen to be similar to the calibration conditions of the EPIDs at MAASTRO CLINIC [20, 21, 22] at 2.5 cm below the water surface which is positioned at 147.5 cm from the target, resulting in an effective source to detector distance (SDD) of 150 cm. An overview of the measurement set-up and equipment is shown in table 5.1 and in figure 5.1. The accuracy of the point measurements is estimated to be within 0.4%.

Two-dimensional measurements

Measuring a complete two-dimensional (2-D) dose distribution can be done with an EPID or film. These measurements both require an additional step (calibration) to convert the measured grayscale values to dose. To avoid these measurements, 2-D dose distributions are obtained using a linear detector array[1] with 23 ionization chambers equally spaced at 2 cm. With this detector array, a 2-D dose distribution could be scanned, with a grid spacing of 2 cm across the entire plane. A reference detector is placed in the field to compensate for fluctuations in dose rate of the linear accelerator. Because the profiles measured are relative, also an absolute point measurement is done at the beam axis.

Possible variations in detector response with time are estimated by comparing two measured dose distributions acquired approximately one hour after another; maximum differences of 0.91% in the gradient area of the treatment fields.

[1]The detector array is a Wellhofer Scanditronix CA24 linear detector array consisting of 23 ionization chambers, read out by a Wellhofer Scanditronix MD240 electrometer.

Table 5.1: Measurement equipment.

Water Phantom	
Water Phantom Type	Scanditronix Wellhöfer Blue Phantom
Scanning volume	$480 \times 480 \times 410$ mm^3
Water surface (SSD)	147.5 cm
Point Detector	
Type	Scanditronix Wellhöfer CC 13
Detector	Ionization chamber
Electrometer	Scanditronix Wellhöfer CU500e
Depth	2.5 cm (SDD=150 cm)
Array Detector	
Type	Scanditronix Wellhöfer CA 24
Detector type	23 ionization chambers spaced equally at 2 cm
Electrometer	Scanditronix Wellhöfer MD240
Depth	2.5 cm (SDD=150 cm)
Phantom Material	
Material	Polystyrene (PS-ABS)
Area	29cm×29cm
Thickness	4.3, 8.6, 12.9, 17.1 and 21.4cm
Density ρ	1.01 – 1.04 g/cm^3
Material	Cork
Area	29cm×29cm
Thickness	1 – 12 cm
Density ρ	$\pm$ 0.2 g/cm^3

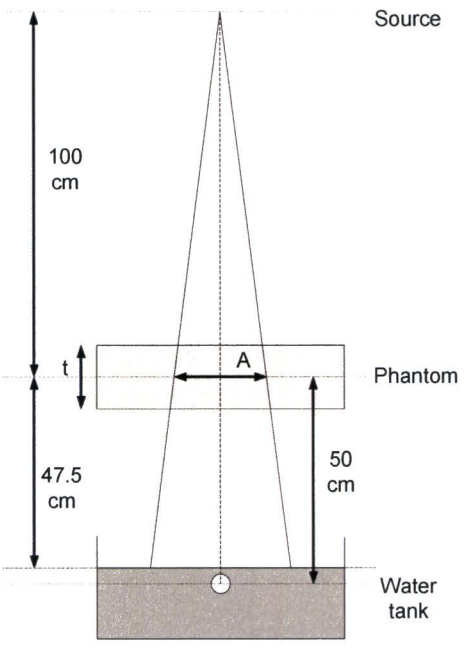

Figure 5.1: The set-up for the point measurements. The detector is placed 2.5 cm below the water surface and can be moved in the water phantom to measure also off-axis point dose values.

EPID measurements

EPID measurements are performed with a video-based EPID, the Theraview-NT. The accuracy of the measurements is estimated to be within 1% on the beam axis and increasing up to 4.5% off-axis [21]. The acquisition of EPID images prior to and during treatment is standard procedure at MAASTRO CLINIC for all curative treatments. The acquisition of these EPID images is part of a quality control program.

5.1 Input parameters for the model

Attenuation coefficient

To measure the effective attenuation, point measurements are taken at on- and off-axis locations r relative to the beam axis with a polystyrene phantom of thickness t placed in the beam and field sizes A of 3×3, 4×4 and 5×5 cm^2 centered around the on- and off-axis locations. The on- and off-axis distances expressed at the isocenter plane are 0, 3, 6 and 9 cm; the polystyrene phantom thicknesses used are 4.3, 8.6, 12.9, 17.1 and 21.4 cm. The primary transmission $T^P(\mathbf{r},t)$ is estimated by extrapolating the measured total transmission $T(\mathbf{r},t)$ to a field size of 0×0 cm^2, the scatter contribution is assumed to be zero for a field size of 0×0 cm^2:

$$T^P(\mathbf{r},t) = \lim_{A \downarrow 0} T(\mathbf{r},t). \tag{5.1}$$

The extrapolation is done by taking a first order linear fit through the measured data and evaluate the transmission at zero field area. The primary transmission profile $T^P(\mathbf{r},t)$ is related to the phantom thickness by the effective attenuation coefficient $\mu(r,t)$:

$$T^P(\mathbf{r},t) \quad = \quad e^{-\mu(r,t)\cdot t}. \tag{5.2}$$

Morton et al [33] used a point by point quadratic calibration for the estimation of the effective attenuation coefficient, i.e. $\mu(\mathbf{r},t) = A(\mathbf{r}) + B(\mathbf{r})\cdot t$. In this report the attenuation coefficient is not fitted to such parameters A and B. Instead of this, the thickness is derived by a two-dimensional interpolation of the measured set of on- and off-axis transmission data.

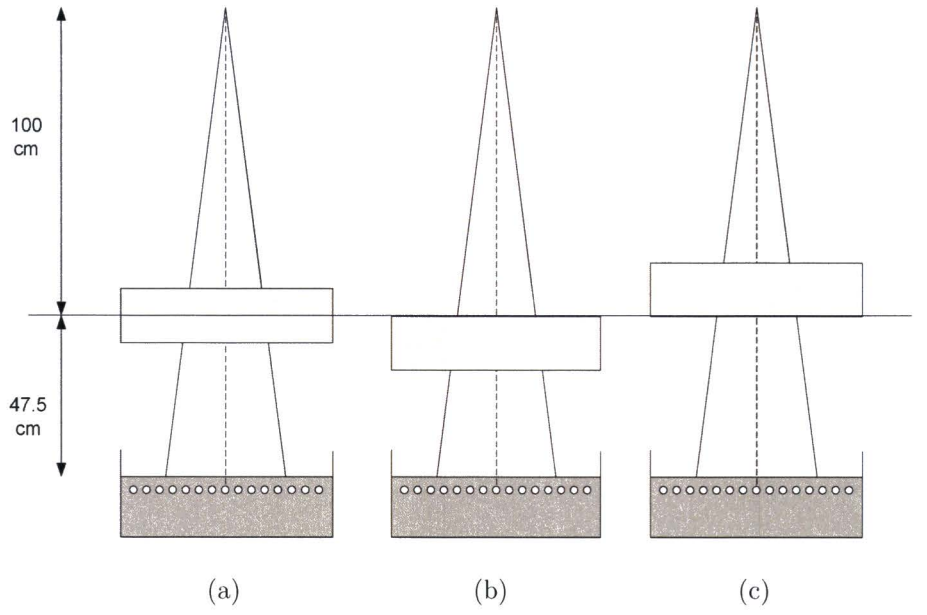

Figure 5.2: The three extreme placements of the phantoms are shown. In (a) the isocenter is located in the center of the phantom (i.e. the midplane), in (b) and (c) the isocenter is at the upper and lower side of the phantom, respectively.

Calculation of the scatter kernels

Point measurements are performed to calculate scatter kernels using the following field sizes: 3×3, 6×6, 10×10, 15×15, 21×21 and 24×24 cm^2, and for polystyrene phantom thicknesses: 4.3, 8.6, 12.9, 17.1 and 21.4 cm. All possible combinations are measured. Also dose measurements are performed without a phantom in the beam for the calculation of the transmission. The total on-axis transmission is defined as the ratio of the dose measured with a phantom in place and without the phantom (so-called open beam). Also an open beam profile is measured along the diagonal of the largest field (24×24 cm^2) by moving the ionization chamber through the water phantom. The kernels are derived using the procedure described in section 4.4.2. The phantom is placed symmetrically around the isocenter resulting in a fixed center-of-mass to detector distance of 50.0 cm.

Verification of the derived kernels

To verify the derived kernels, on-axis point transmission measurements are done for a set of rectangular fields: 5×20, 10×20, 20×5 and 20×10 cm^2. The same phantom thicknesses are used as for the fit: 4.3 – 21.4 cm. The function used to verify the three kernels is the same as the fitting function but with the appropriate boundary values of the integral in eq. (4.5).

Scatter kernels for other air gaps

To analyse the influence of the position of the phantom on the shape of the scatter kernels, point measurements are performed for other phantom detector distances. The phantom is not placed symmetrically around the isocenter but with the upper and the lower sides of the phantom placed at the isocenter (see figure 5.2). This is done for the phantoms with thickness 8.6 cm and 17.1 cm. The resulting distances from phantom midplane to detector (MDD) are 45.7, 50.0 and 54.3 cm for the 8.6 cm phantom. And for the 17.1 cm thick phantom: 41.5, 50.0, and 58.6 cm.

5.2 Homogeneous phantoms

To assess the accuracy of the model, first homogeneous phantoms are investigated because the homogeneous phantoms best represent the fitting geometries.

Off-axis point measurements

To verify the prediction model the measured transmission and the predicted transmission values are not only compared for on-axis distances but also for off-axis distances. Point measurements are performed at off-axis distances of 0, 3, 6 and 9 cm along the longest field axis and for polystyrene phantom thicknesses of 4.3, 8.6, 12.9, 17.1 and 21.4 cm. The field sizes used are 5×24 and 15×24 cm^2.

Asymmetric field

For the evaluation of the prediction algorithm in case of an asymmetric field, two homogeneous phantom thicknesses are used. Phantom thicknesses are 8.6 and 17.1 cm of polystyrene. The midplane of the phantom is placed at the isocenter plane, situation (a) in figure 5.2. The field size is 7.5×24 cm^2, graphically shown in figure 5.3. Measurements are performed with the linear detector array.

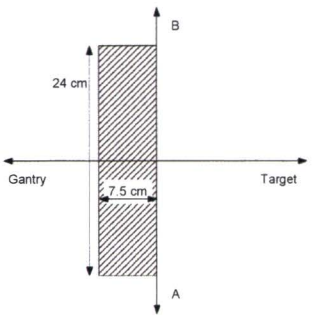

Figure 5.3: Asymmetric field size.

Different air gaps

The phantoms can be placed symmetric or asymmetric relative to the isocenter plane, see figure 5.2. Two homogeneous polystyrene phantoms are used with a thickness of 8.54 and 17.12 cm, H1 and H2 respectively. To make an estimation of the error, three positions of the phantoms are investigated: (a) the midplane of the phantom is coinciding with the isocenter plane, (b)/(c) the upper/lower side of the phantom is coinciding with the isocenter plane, see figure 5.2. The midplane to detector distance (MDD) for situation (a) is 50 cm, the same as the fitting geometry. The MDD for situation (b) (the minus sign) and (c) (the plus sign) is 50 ± 4.27 cm and 50 ± 8.56 cm, for H1 and H2 respectively. The field size irradiating the phantoms is 15×24 cm^2. The measurements are done with the linear detector array.

5.3 Inhomogeneous phantoms

To simulate clinical treatment situations, also phantoms with inhomogeneities are investigated. The phantoms are made out of polystyrene and cork, see table 5.1 for details. Five phantoms are investigated, a schematic view of the phantoms is shown in figure 5.4. The phantoms can be classified according to the midplane symmetry; phantom A, C and D are midplane symmetric and phantom B1 and B2 are midplane asymmetric. All the measurements are performed with the linear detector array to make a two dimensional dose distribution and the field size used to irradiate the phantoms is 15×24 cm^2.

Midplane symmetric

First phantom D is investigated. This phantom consist of two large inhomogeneities of 6.2 cm cork (low electron density) separated by a polystyrene layer of 4.3 cm. On top and beneath the cork is a layer of 2.1 cm polystyrene. This phantom is used to simulate the lungs in a patient; these have a smaller density than the surrounding tissue. The phantom is placed with the midplane coinciding with the isocenter plane.

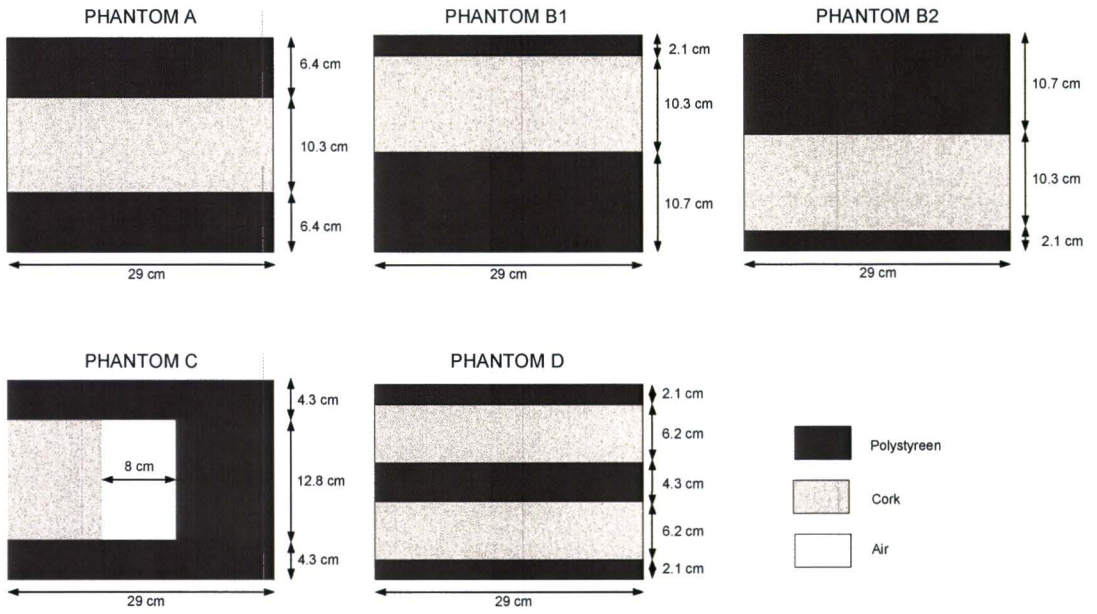

Figure 5.4: The phantoms A-D are made of polystyrene and cork. The phantoms are all symmetric in the direction perpendicular to the plane of drawing. The field size irradiating the phantoms is 15×24 cm^2; the phantoms are placed in the beam with the geometrical midplane positioned in the isocenter.

Midplane asymmetric

Deviations from the midplane symmetry are assessed with the phantoms A, B1 and B2. Phantom A is midplane symmetric and consists of a layer of 10.3 cm cork embedded between two layers of 6.4 cm polystyrene. Phantom B1 consists of the same layer of cork but now the layer of polystyrene on top of the cork is 2.1 cm and the layer below the cork is 10.7 cm thick. Phantom B2 is similar to B1 but the two layers of polystyrene are reversed: 10.7 cm on top and 2.1 cm below the cork. The geometrical midplane is located in the isocenter plane for all three phantoms. This means that for phantom B1 the center-of-mass is shifted towards the detector and for phantom B2 towards the target.

3 Slab phantom

To create steep dose gradients in the portal dose distributions, a three slab phantom is created. This phantom consists out of two layers of 4.3 cm polystyrene and between these two layers there are three regions with a different electron density; the thickness of the region is 12.8 cm. Symmetrical around the center axis of the phantom, there is a cavity of air of 8 cm width, to the left a slab of cork and to the right a slab of polystyrene. This phantom is also placed with the midplane of the phantom coinciding with the isocenter plane.

5.4 Clinical data: breast cancer treatment

The clinical case presented in this report is the treatment of a breast cancer patient. The patient is treated with both wedged and non-wedged beams; only the non-wedged beams have been taken into consideration because portal dose images with wedged beams cannot be predicted by the model. The treatment consists out of two fields directed opposed to each other. EPID images are acquired with and without patient in the beam. The calculation of the EHP is done by ray tracing through the CT-scan of the patient. For one of the non-wedged fields, an EPID image is predicted and compared to the measured distribution. The field size used is 11.1×16.2 cm^2 and

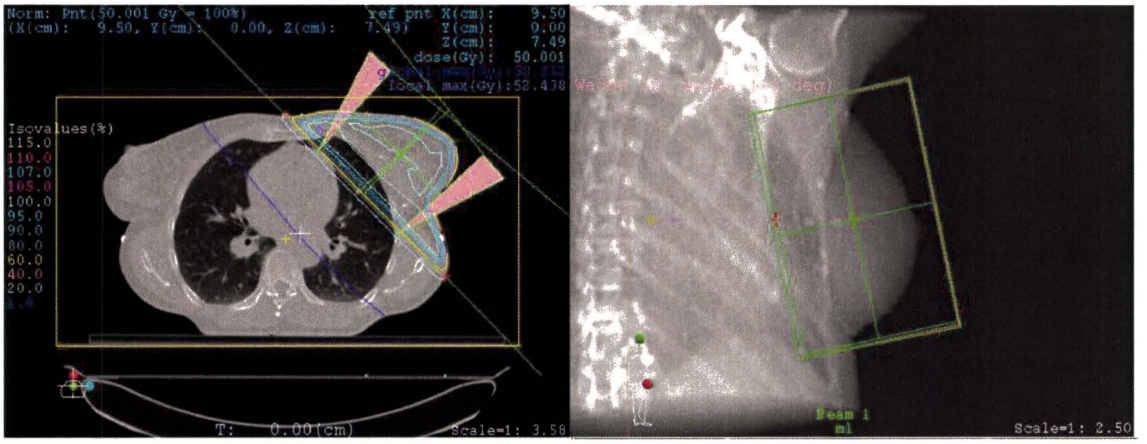

Figure 5.5: The treatment planning system (XiO, CMS, St. Louis (MO), USA) calculates the dose distribution in the patient. Isodose lines are plotted on top of the CT-scan of the patient (right plot). The plot on the left shows the field size superimposed on the digitally reconstructed radiograph (DRR).

a collimator rotation of 258°. The water equivalent thickness at the center of the EPID can be extracted from the treatment planning system and is estimated to be 9.74 cm.

Table 5.2: Overview of the measurements.

Section	Subsection	Field size [cm×cm]	Phantom	Thickness [cm]	Isocenter symmetric	Midplane symmetric	Detector Type
Input parameters	Attenuation coefficient	3×3, 4×4 and 5×5	Polystyrene	4.3, 8.6, 12.9, 17.1 and 21.4	Yes	Yes	Point
	Fit kernel	3×3, 6×6, 10×10, 15×15, 21×21, 24×24	Polystyrene	4.3, 8.6, 12.9, 17.1 and 21.4	Yes	Yes	Point
	Kernel verification	5×20, 10×20, 20×5 and 20×10.	Polystyrene	4.3, 8.6, 12.9, 17.1, and 21.4	Yes	Yes	Point
	Kernels for other air gaps	3×3, 6×6, 10×10, 15×15, 21×21, 24×24	Polystyrene	8.6 and 17.1	No	Yes	Point
Homogeneous Phantoms	Verification of model	5×24, 15×24.	Polystyrene	0, 4.3, 8.6, 12.9, 17.1, and 21.4	Yes	Yes	Point
	Asymmetric field	7.5×24	Polystyrene	8.6 and 17.1	Yes	Yes	Array
	Different air gap	15×24	Polystyrene H1 and H2	8.6 and 17.1	No	Yes	Array
Inhomogeneous Phantoms	Midplane symmetric	15×24	D		Yes	Yes	Array
	Midplane asymmetric	15×24	A, B1, B2		Yes No	Yes Yes	Array Array
	3 Slab phantom	15×24	C		Yes	Yes	Array
Clinical Study		11.1×16.2	Patient data CT - scan		No	No	EPID

Chapter 6

Results of the Prediction Model

This chapter describes the results of the measurements presented in chapter 5. The numbering of the sections is the same as in chapter 5. The results of the measurements are presented along with a short discussion of the particular measurement. The general discussion of the total prediction model with the conclusions is shown in chapter 7. Unless stated otherwise, the results in this chapter are expressed as mean $\pm$ 1 standard deviation (SD). Differences of a measurement M relative to a standard G is for absolute differences expressed as $M - G$ and for relative differences as $(M-G)/G$. Accuracies are expressed as the mean relative differences. Field sizes are expressed at the isocenter planes and results for the portal plane predictions and measurements are expressed in portal plane coordinates, radiological thickness is expressed as polystyrene equivalent thickness.

6.1 Input parameters for the model

6.1.1 Attenuation coefficient

In figure 6.1(a), the logarithm of the primary transmission is plotted against the polystyrene phantom thickness. The dotted line shows the ideal exponential decay if the beam was mono-energetic, the attenuation coefficient of this dotted line can be calculated using eq. (2.2) and is estimated to be 0.048 cm^{-1}. The deviation from this dotted line shows the decrease of the attenuation coefficient (beam hardening) due to the heterogeneous energy spectrum of the 6 MV photon beam.

In figure 6.1(b) the change in primary transmission for the off-axis points is shown. The primary transmission is normalized at the beam axis to show the difference with the off-axis points relative to the on-axis transmission. The attenuation coefficient increases (beam softening) for large off-axis distances resulting in a lower primary transmission relative to the beam axis due to a lower mean energy of the photon beam.

The results presented in figure 6.1 are also shown numerically in table 6.1. The point measurements for the individual measurements are shown in the table B.1 of appendix B.

6.1.2 Calculation of the scatter kernels

The results for the transmission measurements are shown in figure B.1(a) of appendix B. The on-axis transmission is defined as the ratio of the dose measured with and without phantom.

The beam profile is measured along the diagonal of the largest field: 24×24 cm^2. This profile is normalized at the beam axis and shown in figure B.1(b). Raw data is in table B.2 of the appendix B.

The on-axis transmission measurements along with the open beam profile are the input for the fitting procedure described in section 4.4.2. The derived pencil beam scatter kernels for the two

Table 6.1: Primary transmission for various polystyrene (PS) phantom thicknesses for on- and off-axis locations. Open beam values are corrected for the treatment couch in the beam.

PS Thickness	Off-Axis Distance			
[cm]	0 cm	3 cm	6 cm	9 cm
0.0	1.0000	1.0000	1.0000	1.0000
4.3	0.8125	0.8155	0.8127	0.8097
8.6	0.6673	0.6686	0.6634	0.6567
12.9	0.5490	0.5497	0.5464	0.5369
17.1	0.4567	0.4561	0.4507	0.4430
21.4	0.3803	0.3790	0.3747	0.3665

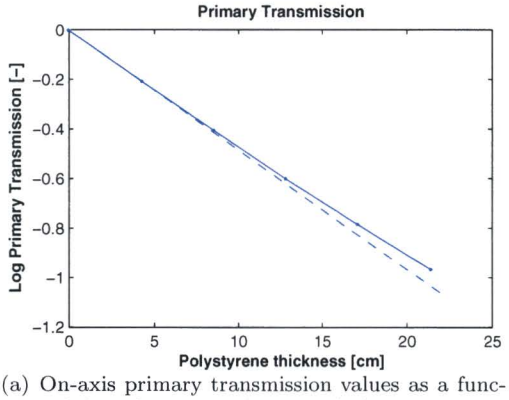

(a) On-axis primary transmission values as a function of the polystyrene phantom thickness.

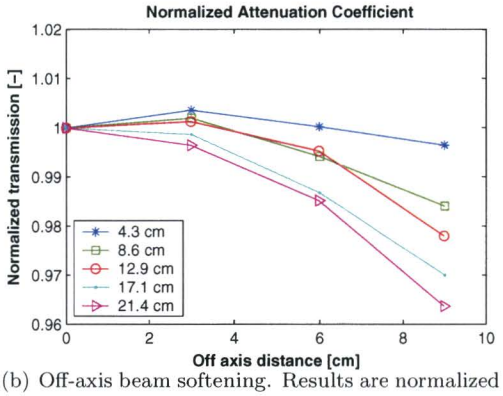

(b) Off-axis beam softening. Results are normalized at the beam axis.

Figure 6.1: Primary transmission as a function of phantom thickness (a) and normalized off-axis transmission, normalized at the beam axis (b). The dashed line through plot (a) represents the ideal attenuation for a mono-energetic beam, deviations from this line show the decrease in attenuation coefficient.

approaches, the parallel and the kernel tilting approach, are shown in figure B.2 of appendix B and figure 6.2, respectively. In these two figures the three kernel functions: Isotropic, Gaussian, and the Klein-Nishina function are shown along with the residual difference of the fit. This residual difference is the relative difference of the calculated/fitted transmission compared with the measured transmission. The fitted coefficients of the different scatter kernels are shown in table B.3 and B.4. The maximum beam width used for the fitting procedure is 24 cm, this results due to beam divergence in a distance off-axis of 18 cm. The kernel values for distances larger than 18 cm are extrapolated from the coefficients of the scatter kernel that are fitted in the region 0 – 18 cm.

The kernels can be fitted to the measured data within 0.2% of the measured value, except for the Klein-Nishina kernel in the tilting approach. This kernel shows differences up to 0.4%, see figure 6.2f. The Klein-Nishina kernel has only one fitting parameter: the amount of scatter at the beam axis. The width of the kernel is defined by the Compton differential cross section and is kept fixed to represent a 6 MV photon beam. This kernel in the tilting approach is probably not a good description of the scatter kernel, based on the deviations of the shape from the other to two kernels and the higher error of the fit.

The Gaussian scatter kernel in the parallel approach for a phantom thickness of 4.3 cm shows a deviation from the other kernels. This can be due to the low amount of scatter that is created from the thinnest phantom resulting in a low scatter to primary signal. Because of this low scatter signal the fit is very sensitive to errors in the measured signal.

The shape of the kernels is interesting. If the scatter kernels are calculated with the parallel approach the scatter distribution will be higher towards the beam axis but fall off faster compared to the kernel tilting approach. To make a quantitative comparison between the different kernels the width of the kernels and the magnitude are investigated. The width of the various kernels can be expresses as the Half Width at Half Maximum (HWHM) and the magnitude is defined as the on axis scatter transmission. The magnitude and HWHM for the different kernels are shown in table 6.2.

The magnitude is increasing with phantom thickness. This is due to the increased amount of scatter that is created by the primary beam because there is more phantom material. The amount of scatter gradually levels off with larger phantom thicknesses due to the loss of intensity of the primary beam and the attenuation of the scattered photons becomes larger than the generation of new scattered photons by the weakening primary beam [26].

The HWHM decreases for larger phantom thicknesses. This decrease in HWHM is a result of two effects. The first effect is that the beam hardens for larger phantom thicknesses (increase in mean energy) and the scatter is more forward peaked for higher energies. The second effect is that the air gap is smaller for larger phantom thicknesses and the angular spread of scatter photons is thus smaller. This HWHM also explains why the Klein-Nishina kernel in the parallel approach has almost the same accuracy of the fit as the other two kernels. The shape, defined mainly by the magnitude and width, of the three kernels is almost identical. In the kernel tilting approach this does not hold for the Klein-Nishina kernel with the parameter $z = 50$ cm, see eq. (4.8). The fit cannot be made within 0.2% and shows a systematic trend error. However if this parameter is adjusted to the (non-physical) value of $1.5 \cdot 50 = 75$ cm, and the fit is done again, then the HWHM increases to 28.46 cm and the kernel difference between measurement and fit is again similar to figure B.2f.

Concluding, the magnitude first increases rapidly with phantom thickness and levels off for larger phantom thickness. The HWHM decreases with phantom thickness due to the increase in mean energy of the beam and the smaller air gap between phantom and detector.

6.1.3 Verification of the derived kernels

In figure 6.3 the differences are plotted between the calculated and the measured transmission. In this plot, the values for measured field sizes 5×20 cm^2 and 20×5 cm^2 are combined as well as the values for 10×20 cm^2 and 20×10 cm^2. This to average out any fluctuations in the measured data

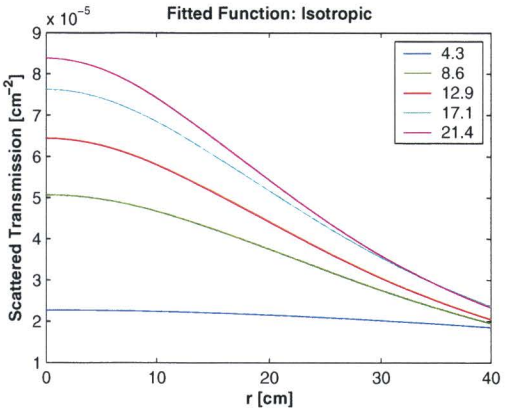

(a) Isotropic kernel.

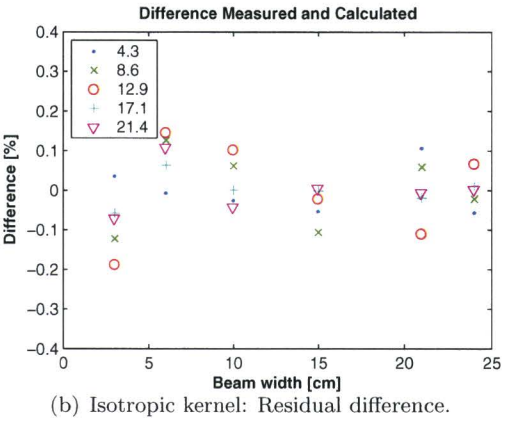

(b) Isotropic kernel: Residual difference.

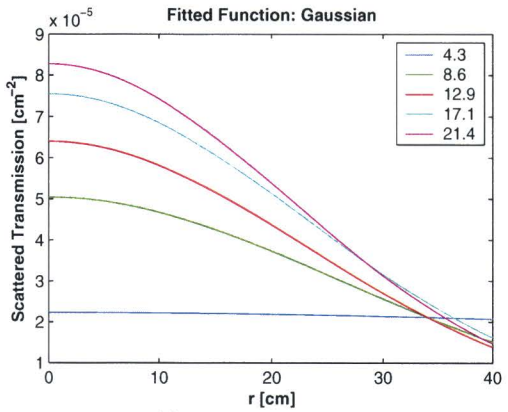

(c) Gaussian kernel.

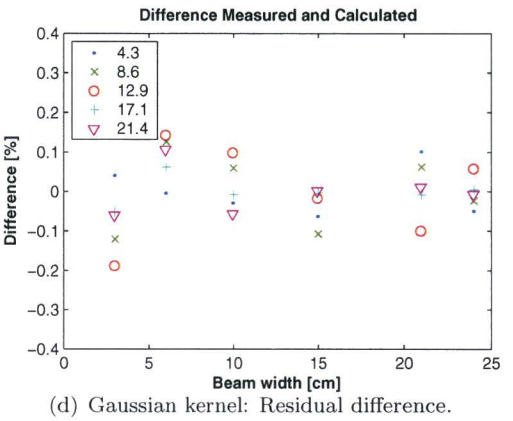

(d) Gaussian kernel: Residual difference.

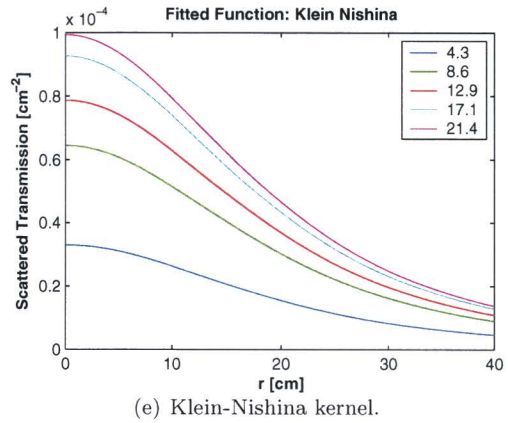

(e) Klein-Nishina kernel.

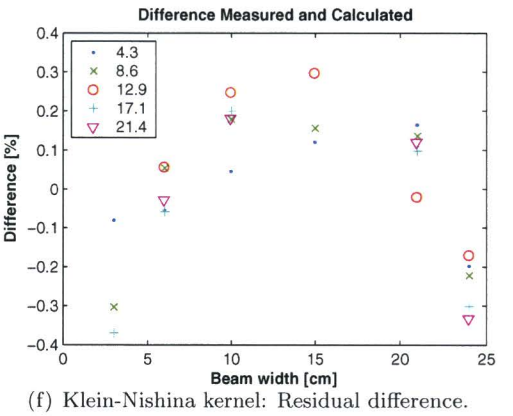

(f) Klein-Nishina kernel: Residual difference.

Figure 6.2: Tilted approach: Fitted kernels (left) and the residual difference of the measurements from the fit (right) expressed as a percentage.

Table 6.2: The magnitude and the Half Width at Half Maximum (HWHM) for the three kernels in the parallel and the tilted approach[1].

Parallel approach

Thickness [cm]	Isotropic Magnitude [10^{-4} cm^{-2}]	Isotropic HWHM [cm]	Gaussian Magnitude [10^{-4} cm^{-2}]	Gaussian HWHM [cm]	Klein-Nishina Magnitude [10^{-4} cm^{-2}]	Klein-Nishina HWHM [cm]
4.3	0.516	47.09	0.503	81.39	0.609	18.97
8.6	1.141	21.67	1.135	20.29	1.187	18.97
12.9	1.450	19.14	1.442	18.01	1.449	18.97
17.1	1.716	18.87	1.700	17.93	1.706	18.97
21.4	1.887	17.68	1.864	16.96	1.830	18.97

Kernel tilting approach

Thickness [cm]	Isotropic Magnitude [10^{-5} cm^{-2}]	Isotropic HWHM [cm]	Gaussian Magnitude [10^{-5} cm^{-2}]	Gaussian HWHM [cm]	Klein-Nishina Magnitude [10^{-5} cm^{-2}]	Klein-Nishina HWHM [cm]
4.3	2.278	80.42	2.235	122.52	3.297	18.97
8.6	5.072	32.51	5.043	30.45	6.449	18.97
12.9	6.444	28.72	6.408	27.02	7.874	18.97
17.1	7.628	28.30	7.556	26.91	9.272	18.97
21.4	8.387	26.52	8.285	25.44	9.944	18.97

The relation between fitting parameters and HWHM: $\mathrm{HWHM}_{Isotropic} = c_2(t)\sqrt{4^{1/3}-1}$, $\mathrm{HWHM}_{Gauss} = \sqrt{\frac{\ln 2}{c_2(t)}}$ and $\mathrm{HWHM}_{Klein-Nishina} = 18.97$ cm.

[1] Note that the parallel and the kernel tilting approach are equal once a lateral scaling factor (1.5) and the magnitude scaling factor (1.5^2) is taken into account. This off course does not hold for the Klein-Nishina kernel because the width is taken as a constant for this kernel.

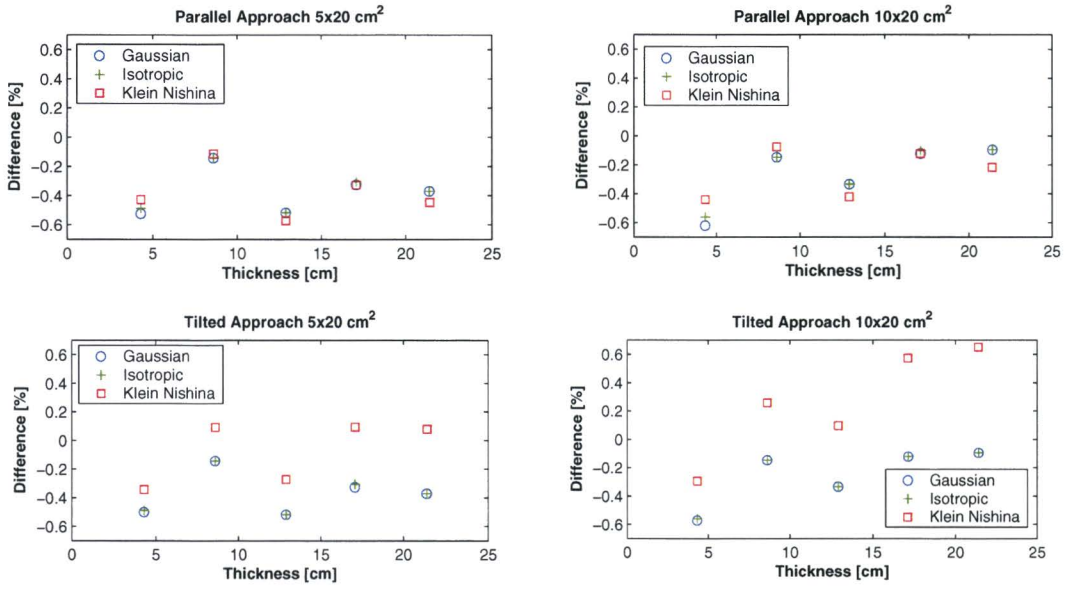

Figure 6.3: Verification of the derived kernels. Difference between calculated and measured *on-axis* transmission values in case of rectangular fields.

by assuming a radial symmetry of the photon beam. The results of the raw measurements as well as the prediction of the on-axis transmission are shown in table B.5 of appendix B.

The differences between predicted and measured transmission values are small and comparable for the two approaches. There is a systematic under-estimation of the fit of 0.3% but this is within the measurement accuracy of the point detector.

6.1.4 Scatter kernels for other air gaps

To analyse the influence of the phantom position on the shape of the scatter kernels, measurements are done for other phantom detector distances.

Kernels are derived for the Gaussian fit function and the tilted approach, kernels for the other two fitting functions are comparable to the Gaussian kernel. Results are shown in figure 6.4(a) and 6.4(c) for the 8.6 and the 17.1 cm phantom respectively. The accuracy of the fit is again within 0.2% of the measurements.

As expected when the lower side of the phantom is placed at the isocenter plane (resulting in a larger air gap between phantom and detector) the kernel is wider and there is a lower on-axis scattered transmission (dashed line in figure 6.4). If the phantom is placed with the upper side of the phantom at the isocenter, a smaller air gap between phantom and detector is created. This results in a higher magnitude and the kernel is more sharply peaked in forward direction (dotted line). The magnitude and HWHM are shown in table 6.3.

This behavior can be explained by taking into account the center-of-mass. The scatter in the EHP concept is assumed to be originating from the center-of-mass of the phantom. The scatter kernels for the different MDDs are approximately equal once a scaling factor representing the divergence is taken into account. The scaling factor depends on the distance of the midplane to detector and is $(\mathrm{MDD}/50.0)^2$. This scaling factor is applied to both the magnitude and the HWHM. Figure 6.4(b) and (d) show the scatter kernels as they are scaled for divergence, in table 6.3 the scaled magnitude and HWHM are also shown.

The scaled scatter kernels are approximately equal, this is an important result because it supports the theory of the EHP concept. The scatter that is the result of a pencil beam can be

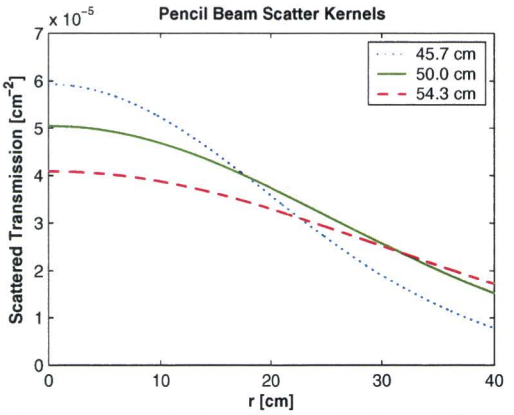

(a) Scatter kernels for phantom thickness 8.6 cm, three midplane to detector distances (MDD).

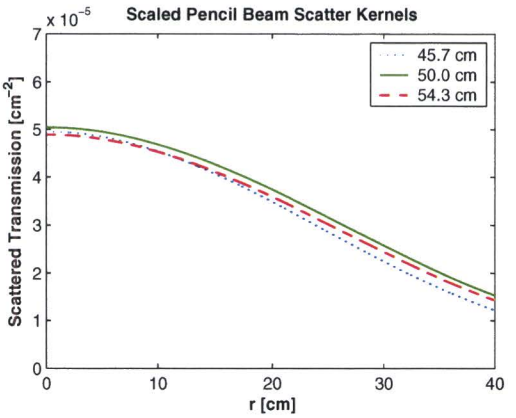

(b) Scatter kernels scaled with divergence to a MDD of 50 cm; Scaling factor is $(45.7/50.0)^2$ and $(54.3/50.0)^2$ for the kernel with a MDD of 45.7 and 54.3 cm, respectively.

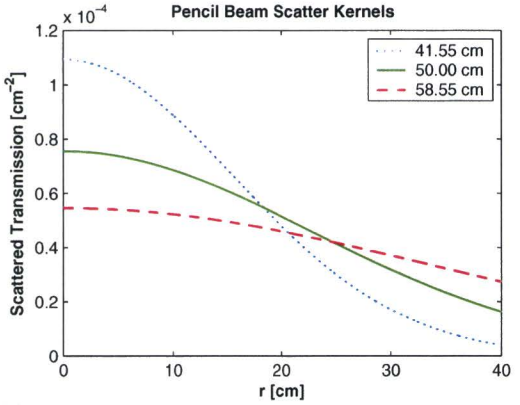

(c) Scatter kernels for phantom thickness 17.1 cm, three midplane to isocenter distances (MDD).

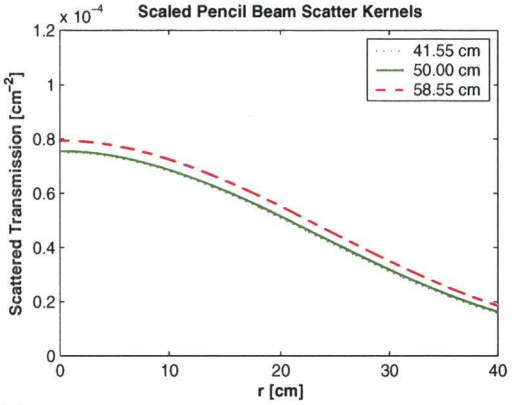

(d) Scatter kernels scaled with divergence to a MDD of 50 cm; Scaling factor is $(41.45/50.0)^2$ and $(58.55/50.0)^2$ for the kernel with a MDD of 41.45 and 58.55 cm, respectively.

Figure 6.4: Gaussian pencil beam scatter kernels (a)/(c) and scaled kernels (b)/(d) for different midplane to detector distances.

Table 6.3: Magnitude and half width at half maximum (HWHM) of the Gaussian kernel in the tilted approach shown in figure 6.4 for varying midplane to detector distances (MDD).

Phantom Thickness [cm]	MDD [cm]	HWHM [cm]	Magnitude [10^{-5}cm^{-2}]	Scaled HWHM [cm]	Scaled Magnitude [10^{-5}cm^{-2}]
8.6	45.7	23.48	5.935	28.10	4.958
8.6	50.0	30.45	5.043	30.45	5.043
8.6	54.3	35.96	4.089	30.04	4.894
17.1	41.5	18.38	10.95	26.75	7.525
17.1	50.0	26.91	7.556	26.91	7.556
17.1	58.6	40.29	5.467	27.69	7.955

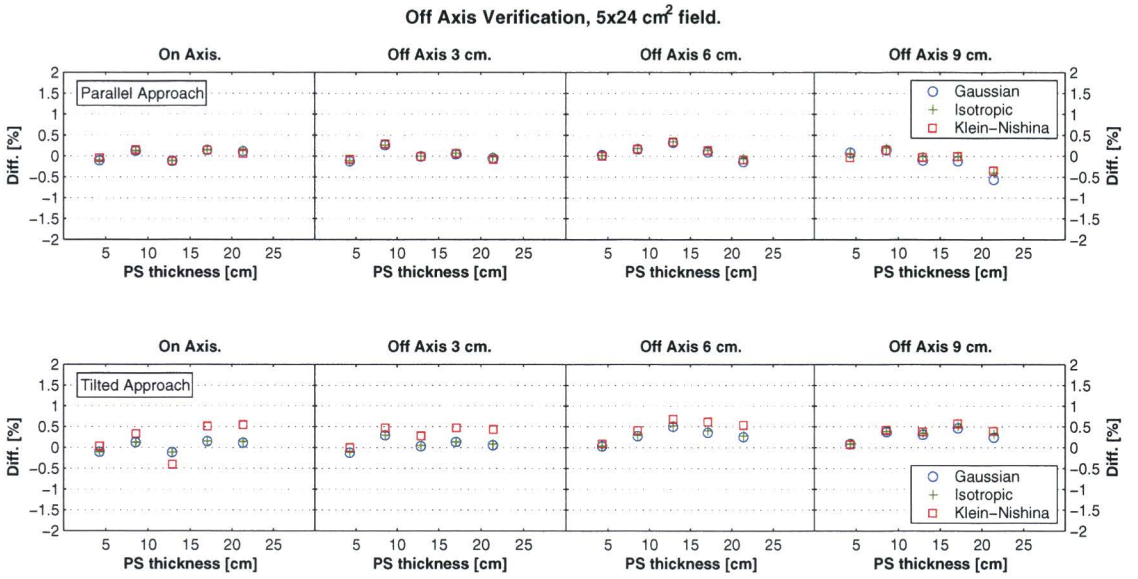

Figure 6.5: Difference calculated and measured on/off axis transmission for the parallel (top) and the tilted (bottom) approach for the field size 5×24 cm^2 for the three fitted kernels. Differences are expressed relative to the measured transmission.

replaced by a point located with the same radiological mass symmetrically distributed around the center of mass along the pencil beam ray line. The scatter can be assumed to originate from that point, the scatter kernels can be calculated for an arbitrary MDD by rescaling it to the new MDD.

6.2 Homogeneous phantoms

6.2.1 Off-axis dependency

The relative differences between calculated and measured transmission values for on- and off-axis positions are graphically shown in figure 6.5 and 6.6. In table B.6 and B.7 of the appendix B, the raw data are shown.

The difference between predicted and measured transmission for both the parallel as well as the tilted approach are small. For the parallel approach, the mean differences averaged over all measurements are $-0.17\pm0.42\%$, $-0.11\pm0.33\%$ and $-0.13\pm0.31\%$ for the Gaussian, isotropic and Klein-Nishina kernels, respectively. For the tilted approach these differences are $0.13\pm0.26\%$, $0.16\pm0.28\%$ and $0.34\pm0.32\%$, respectively.

Looking at these overall results, there is not much differences between the two approaches and the three different kernels. However, if one looks in detail to the individual data points, there are differences in case of the parallel approach. The errors are higher for larger off-axis distances and thicker phantoms. This is most clearly seen for the large field 15×24 cm^2 and for the thickest phantom of 21.4 cm. The scatter contribution is the largest for this configuration, i.e. an on-axis scatter-to-primary ratio of 17%. The parallel approach shows a systematic smaller predicted transmission for the larger fields and larger phantom thicknesses; the errors in total predicted transmission can be as large as 2%. This does not occur for the kernel tilting approach.

The explanation for this larger error is a result of the parallel approach. In this approach the location of the field edge is located 12 cm from the beam axis, while the measuring point is $9 \cdot 1.5 = 13.5$ cm from the beam axis due to divergence. The smaller transmission value is due to the fact that the beam divergence is not included in the scatter dose calculation. The scatter dose is calculated as if it is not dependent on the incident angle of the beam on the photon (see figure 4.3).

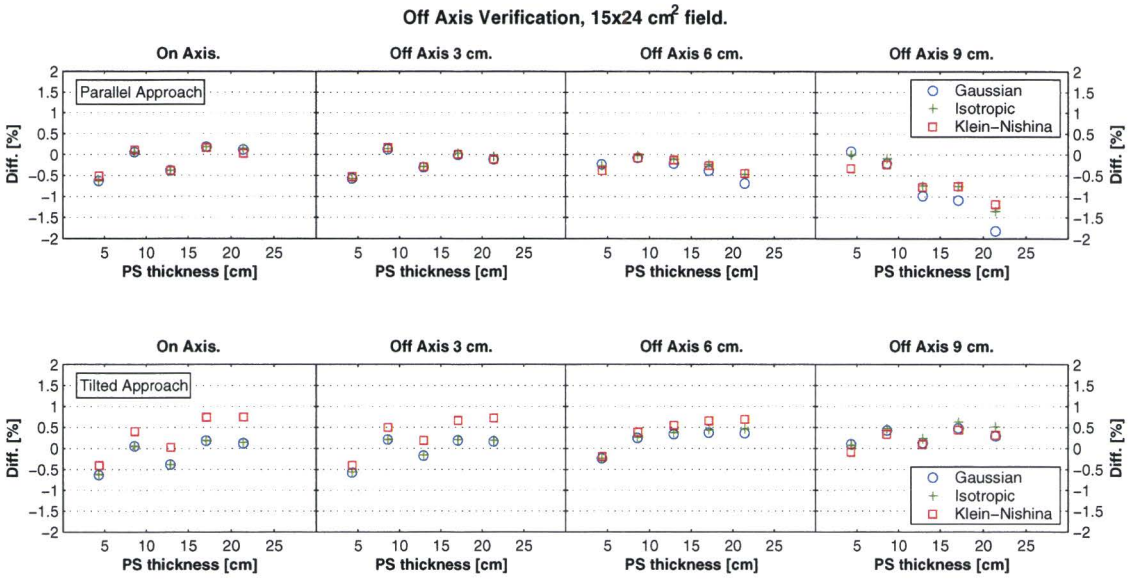

Figure 6.6: Difference calculated and measured on/off axis transmission for the parallel (top) and the tilted (bottom) approach for the field size 15×24 cm^2 for the three fitted kernels. Differences are expressed relative to the measured transmission.

Based on both the on- and off-axis results for the homogeneous phantoms, the kernels in the **tilting approach** in combination with the Gaussian or the isotropic kernel show good agreement with measurement. The shape of the two kernels is approximately the same, no differences in accuracy are expected between these two kernels. The predictions for the other phantoms in this chapter are done with the **Gaussian kernel** in the tilting approach. Based on the differences in figure 6.5 and 6.6, the overall accuracy of the method representing the fitting geometry for homogeneous phantoms is estimated to be within 0.6%.

The results also show that it is not necessary to derive different kernels for off-axis distances. The scatter kernels are fitted to the on-axis transmission measurements but can also be used for off-axis distances. This observation supports the use of the pencil beam concept: the substitution of the incident beam as a superposition of many small pencil beams.

6.2.2 Field symmetry dependency

Results for the asymmetric field are shown in figure 6.7 for two cross-sections of the two-dimensional dose distribution, at y=0 cm and x=5.5 cm.

Differences are calculated along these two cross sections and are smaller than 1%, except for the points placed at steep dose gradients on the field edges (x=−12,−10,−2 and 0 cm), (y=−18, −16 and +18 cm). Differences for the 8.54 cm phantom are 0.17±1.07% and −0.08±0.58% for the x and y profile, respectively; for the 17.12 cm phantom these differences are 0.25±1.29% and −0.17±0.79%. The accuracy is similar to the accuracy presented in the previous section for the homogeneous phantoms with symmetric fields. The accuracy of the model does not depend on field size or the field symmetry.

6.2.3 Air gap dependency

Results of predicted and measured dose distributions are shown in figure 6.8 and 6.9 for phantoms H1 and H2, respectively.

The relative dose differences for phantom H1 and H2 compared to the fitting geometry, situation (a) are x: 0.60±1.40% y: 0.90±0.41%, and x: 0.77±1.41% y: 0.82±0.73% for the H1 and

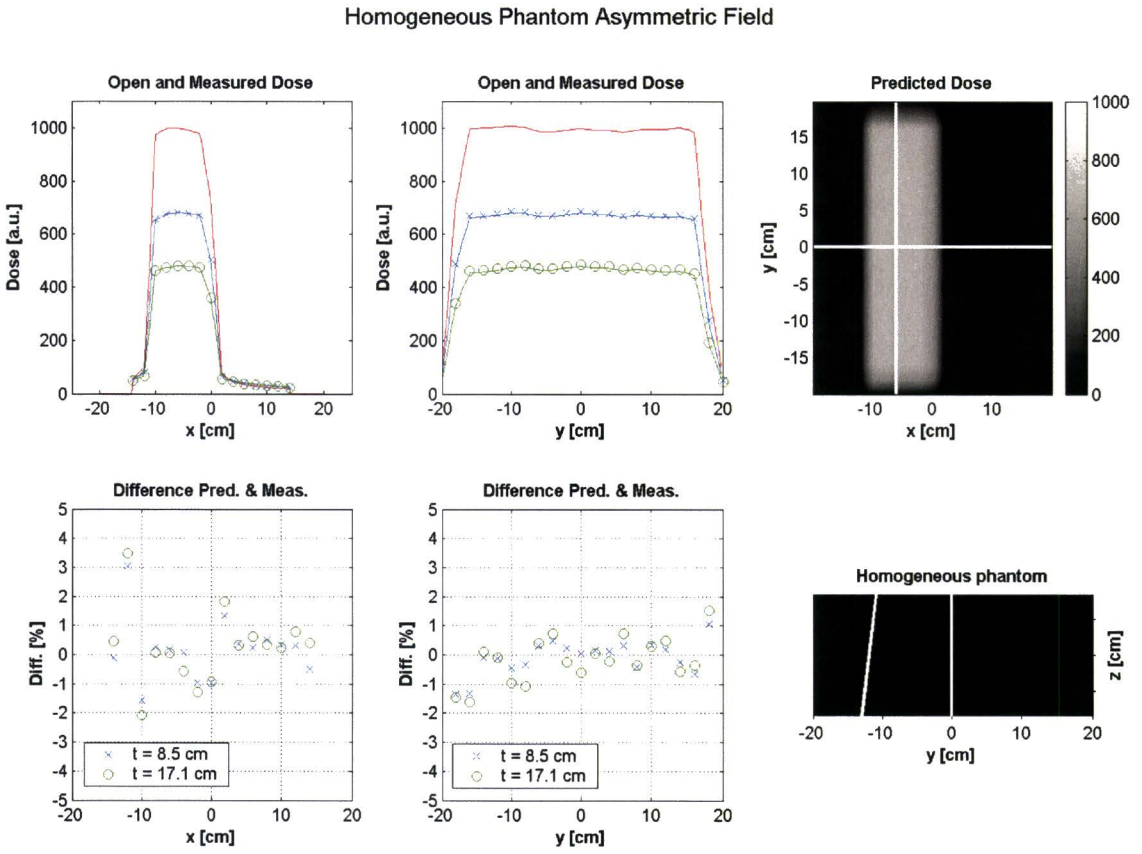

Figure 6.7: Results for the asymmetric field. The lower right plot shows the phantom with two ray lines indicating the field edges. The upper right plot shows the predicted two dimensional dose distribution, the dose along the two indicated lines at y=0 cm and x=5.5 cm is shown in the upper left and middle plot. The upper left and middle plot consist of three lines, from top to bottom these are the open dose profile (solid line), dose profile for the 8.5 cm PS (crosses) and 17.1 cm PS phantom (circles), respectively. Differences in the lower plot are expressed as relative difference between predicted and measured dose normalized to the total on-axis dose.

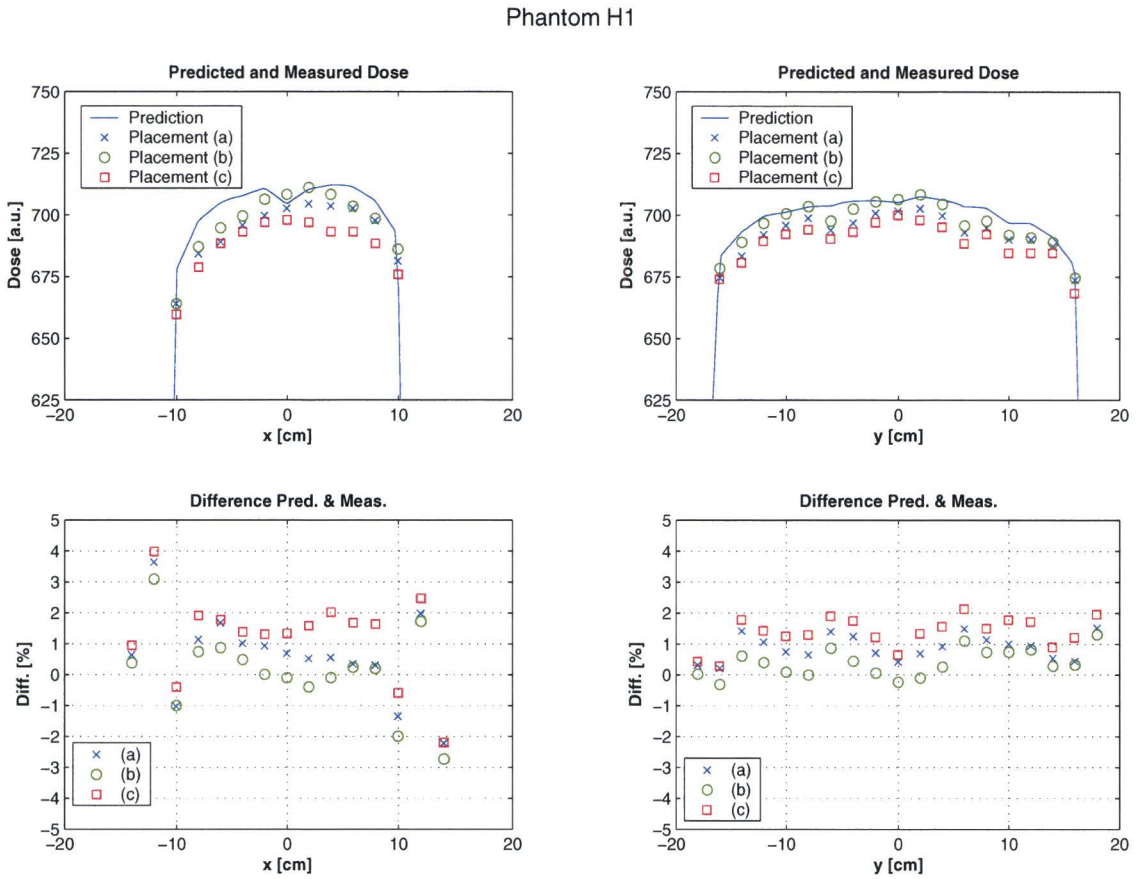

Figure 6.8: Different air gaps between phantom H1 and detector. Phantom thickness is 8.54 cm. In the upper plots two cross sections are shown with the predicted dose (solid), placement (a) (crosses), (b) (circles) and placement (c) (squares). The lower two plots show the difference of the predicted and measured dose relative to the on axis measured dose.

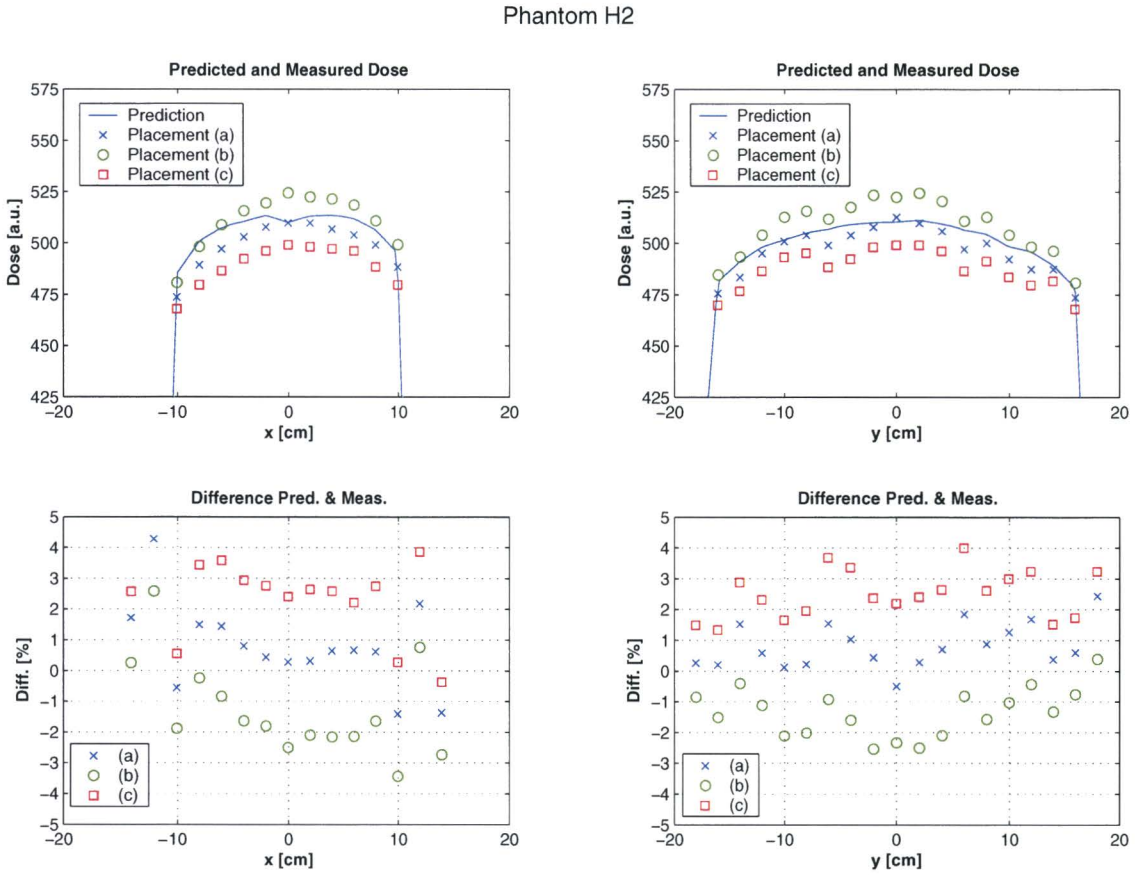

Figure 6.9: Different air gaps between phantom H2 and detector. Phantom thickness is 17.12 cm. In the upper plots two cross sections are shown with the predicted dose (solid), placement (a) (crosses), (b) (circles) and placement (c) (squares). The lower two plots show the difference of the predicted and measured dose relative to the on axis measured dose.

H2 phantom respectively. For the situation (b)/(c) the measured dose is higher/lower than for situation (a) due to the decreased/increased air gap.

For phantom H1 which is the thinnest phantom of the two, the resulting relative differences are small due to the small amount of scatter and the high primary dose, x: 0.10±1.38% y: 0.40±0.45% and x: 1.27±1.44% y: 1.39±0.51% for situation (b) and (c) respectively.

For phantom H2 the thickest phantom of the two, the resulting relative differences are larger due to the higher amount of scatter and the lower total dose, x: −1.30±1.56% y:−1.34±0.80% and x: 2.54±1.52% y: 2.52±0.78% for situation (b) and (c) respectively.

The differences for the situations (b) and (c) can be explained by taking into account the air gap, if the pencil beam scatter kernels are rescaled to take into account the different air gap (as described in section 6.1.4), then the differences are again small, e.g. for Phantom H2 (b) the differences are then 0.35±1.41% and 0.30±0.58%, for the x and y cross-section.

From the errors in the prediction presented above a quick rule of thumb can be developed to estimate the error that is made if the phantoms midplane is not coinciding with the isocenter midplane. This rule of thumb is as follows:

$$\text{Error [\%]} = (\text{PS eq. thickness [cm]} / 8.6\text{ cm}) \times (\text{displacement center-of-mass [cm]} / 10\text{ cm}).$$

The differences of the prediction and the measured dose distribution for situation (a), representing the fitting geometry, can maybe be explained by two factors, first the exact PS thickness can deviate from the used PS thickness. This is estimated to be approximately 1 mm, this results in a dose difference of 0.4%. And second the actual measurement is estimated to be correct within 0.4%.

6.3 Inhomogeneous phantoms

The inhomogeneous phantoms analyzed in this section are made out of polystyrene and cork. The attenuation coefficient for polystyrene is described in section 6.1.1. The attenuation of cork can be related to the attenuation of polystyrene. The attenuation of the cork is estimated in a similar way as described in section 6.1.1, i.e. extrapolation to a field size of 0×0 cm^2. The primary transmission for a slab of cork of 12.4 cm thickness is estimated to be 0.8886, resulting in: 1 cm cork = 0.21 cm polystyrene.

6.3.1 Midplane symmetry dependency

Results for phantom D are shown in figure 6.10 for two profiles located at the coordinates x=0 cm and y=0 cm.

The average differences along the x and y profile are −0.59±1.51% and −0.57±0.63%. The dose difference is generally smaller than 1.5%, except for the areas with steep dose gradients. The a small systematic under-prediction of around −0.6% can maybe be explained by the conversion of the total phantom to equivalent homogeneous (polystyrene) thickness; a difference of −0.6% indicates that that the real polystyrene equivalent thickness is ±2 mm thicker than the used thickness.

This result for the inhomogeneous phantom supports the use of the equivalent homogeneous phantom (EHP) concept: a highly inhomogeneous phantom can be replaced by its equivalent homogeneous thickness.

6.3.2 Midplane asymmetry dependency

Results of measurements in case of phantoms A, B1 and B2 are shown in figure 6.11.

The differences for the midplane symmetric phantom A are small, −0.06±1.43 and −0.02±0.67% for the x and y cross section. This small error is expected because the phantom is midplane symmetric. The errors for the x and y cross section for phantom B1 are −0.35±1.42% and −0.46±0.68%, and for phantom B2 0.64±1.48% and 0.54±0.59%. These results can be explained

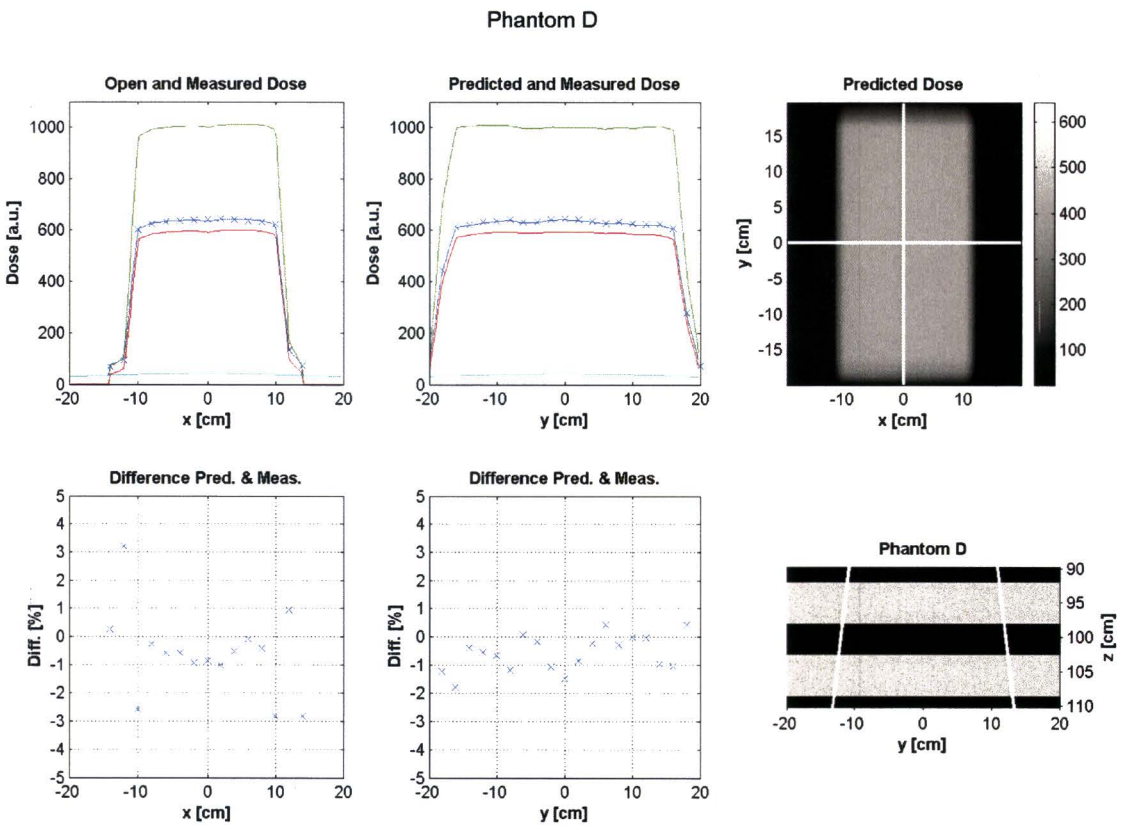

Figure 6.10: Phantom D is shown schematically in the lower right plot. The top right plot shows the predicted dose with superimposed the two cross section examined. These measured dose (crosses) is showed in the upper left and middle plot. The solid represent from top to bottom line: the open beam dose, the predicted dose, primary dose and the scattered dose. The SPR ratio at the beam axis is 0.071. The differences between prediction and measurement are shown in the bottom plots.

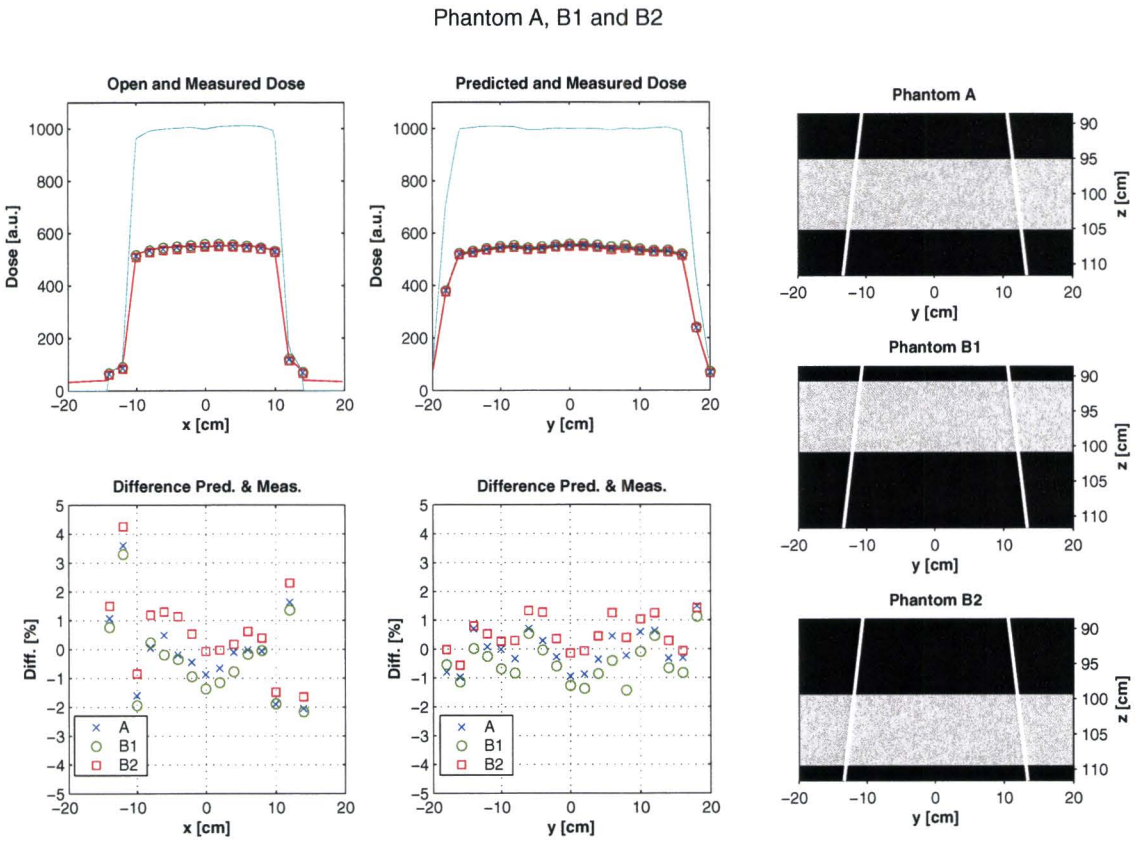

Figure 6.11: Phantom A, B1 and B2 shown on the right consist all of a layer of cork embedded within two polystyrene layers, these layers are different thicknesses for the different phantoms, see figure 5.4. The cross sections along the x and y direction are taken through the beam axis. The differences in the lower plots are expressed relative to the on axis dose.

by taking into account the center-of-mass of the phantom, similar to the results of the homogeneous case presented in section 6.2.3. For phantom B1 this center-of-mass is shifted towards the bottom of the phantom and for phantom B2 shifted towards the upper side of the phantom. For phantom B2 this results in a larger distance of the center-of-mass to detector and the scatter that is assumed to be produced at that point, is spread due to divergence over a larger area of the detector with a lower magnitude. Phantom B1 has a smaller center-of-mass to detector distance so the scatter is more forwardly peaked and higher in magnitude.

The shift in center-of-mass can be calculated and is estimated to be 2.34 cm towards/away from the detector, for phantom B1 an B2. The error in the prediction made for this displacement of the center-of-mass is on average -0.4% and $+0.6\%$ for phantom B1 and B2 respectively. This is in agreement with the rule of thumb for the estimation of the error made for the homogeneous phantoms described in section 6.2.3 that are displaced relative to the detector. The scatter kernels can be rescaled to take into account the new phantom midplane-to-detector distance as described in section 6.1.4; the differences for phantom B1 are for the x and y cross-section 0.40 ± 1.41 and y: $0.27\pm0.66\%$, respectively. For phantom B2 these differences are -0.03 ± 1.49 and $-0.11\pm0.59\%$, respectively for the x and y cross-section.

6.3.3 3 Slab phantom

Results for phantom C are presented in figure 6.12.

For the cross sections (a) – (d) the differences between prediction and measurement are generally smaller than 1% except for the point at the steep dose gradients; (a)-(c): x=-14, -12, -10, 10, 12 and 14 cm, (d): y=-6 and 6 cm. The average values[1] for the cross-sections (a), (b), (c) and (d) are $-0.75\pm0.19\%$, $-0.69\pm0.19\%$, $-0.57\pm0.27\%$ and $-0.67\pm1.86\%$, respectively. The systematic under prediction of around -0.6% is systematic but nevertheless not large and comparable to the accuracy achieved with the homogeneous phantoms.

From the results presented for the inhomogeneous phantoms one can conclude that the model has an accuracy of 2% for the prediction of the portal dose distribution if the phantoms radiological midplane is coinciding with the isocenter plane.

6.4 Clinical study

The final case presented is the treatment of a breast cancer patient. The parameters of the treatment are discussed in section 5.4. The predicted portal dose is shown in the top right plot of figure 6.13. On the left the predicted and the measured dose are shown for two cross sections along the x and y axis. To evaluate the prediction results the differences are not evaluated by a point by point comparison of the dose as was done for the previous results. A frequently used method to compare dose distributions in radiotherapy is the so-called gamma method. This method is also suitable to compare the dose distributions in regions of steep dose gradients. The usual accepted accuracy in radiotherapy is a dose difference smaller than 3%, or in regions of steep dose regions a spatial mismatch of the dose of 3 mm. The gamma method can take into account these both criteria and the mathematical framework is explained in appendix C. The dose criterion is set to 3% maximum dose difference and the spatial criterion is set to 5 mm (this is 3.3 mm in the isocenter plane). The value of γ then expresses the difference. If this value is 0 then the predicted and measured dose are equal in that point, if the value is 1 then either the dose difference is 3% or there is a spatial shift of the dose of 5 mm (or a combination of both, e.g. 2.1 % dose difference with a shift of 3.5 mm).

The predicted dose matches well with the measured dose, i.e. γ-values below 1 over large regions in the portal image. The differences that are measured are in the region where there is no tissue (the two triangular shaped regions around (x,y)=(8,8) and (3,-10)), or at steep gradients in

[1]The values at the steep dose gradients are not included in the average results.

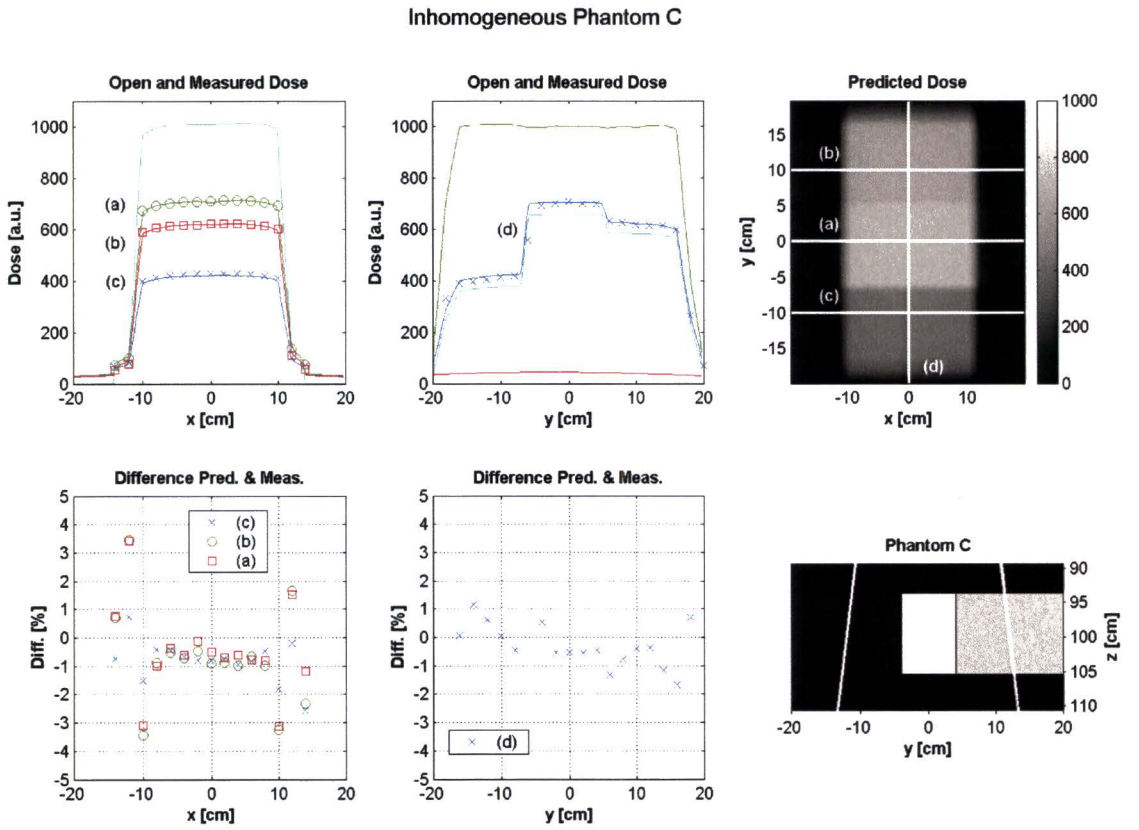

Figure 6.12: Phantom C is shown at the bottom right plot, the upper right plot shows the predicted two dimensional dose distribution with location of the cross sections (a) – (d) that are shown in the left and middle plot. Differences are expressed relative to the on-axis dose. In the upper middle plot the solid lines represent (from top to bottom): open dose, predicted dose, primary dose and scattered dose. The SPR ratio for the intersection points of the cross sections (a), (b) and (c) with cross section (d) are 0.0686, 0.0694 and 0.1162, respectively.

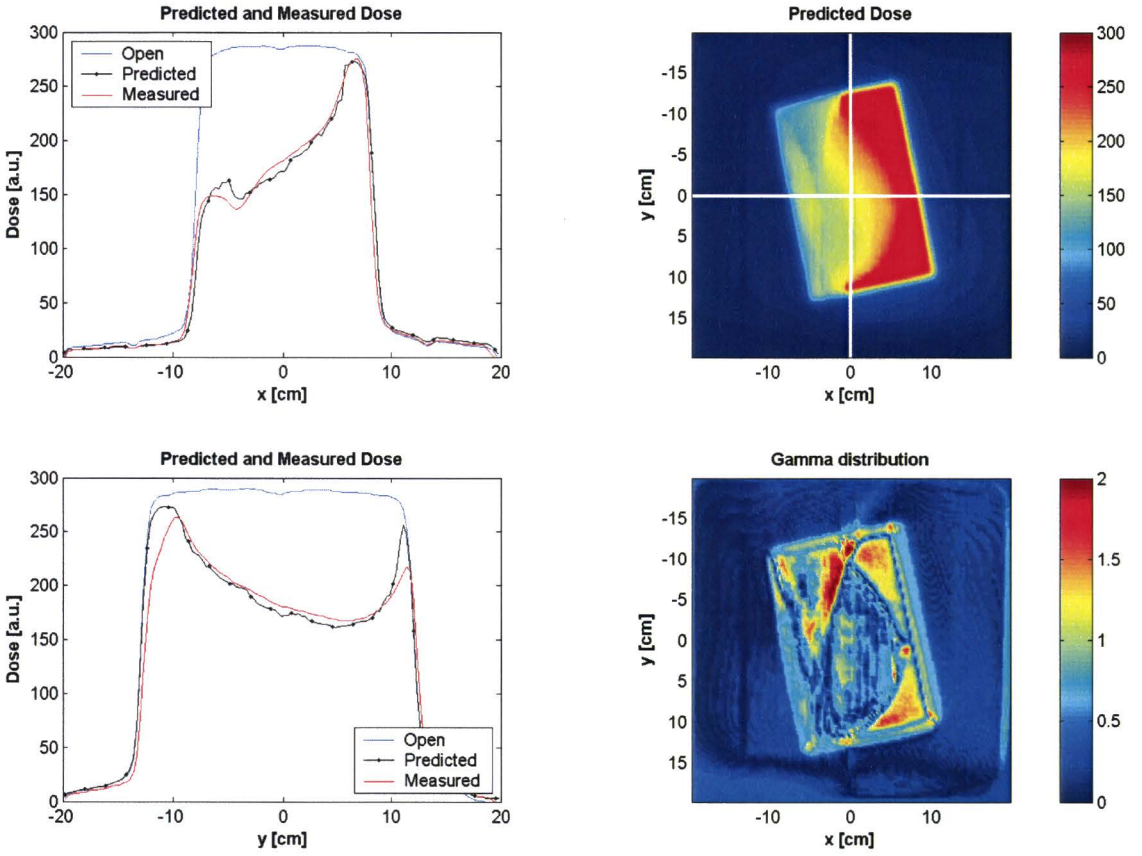

Figure 6.13: Breast cancer treatment. Upper right plot is the predicted portal dose and the two cross sections are shown. The plots on the left show the open beam profile and the predicted (with marker) and measured dose profile. The lower right plot shows the gamma distribution, values smaller than 1 within the accepting criteria (smaller than 3% dose difference or 5 mm spatial difference); higher values indicate a deviation larger than the accepting criteria.

the radiological thickness (around (x,y)=(−2,−7)). The difference in the clinical region of interest is small, γ values below 1, indicating a dose difference of below 3%.

The clinical case is presented to show the feasibility of the method. If there are differences between the prediction and the measurement, these differences are difficult to interpret. Large differences can exist due to a difference in position or deformation of patient anatomy between the reference CT and the actual measurement during treatment.

The prediction of the portal images is estimated to be within 3% of the measured portal dose for large areas of the portal image; differences found are most likely to be due to a different patient position/anatomy during treatment for this clinical case study.

Chapter 7

Discussion and Conclusion

In this chapter, the results derived in the previous chapters will be discussed in general. A detailed discussion about the specific measurements was already presented in the previous chapters. This chapter will give an overview of results in general terms. At the end of this chapter, some conclusions are drawn.

Attenuation coefficient

The attenuation coefficient for on- and off-axis distances is measured for small fields and extrapolated to the transmission at a zero field size. The attenuation coefficient for a specific off-axis distance and thickness is found by interpolation between the measured data points. This interpolation step can be removed by fitting the measurements to a model that takes into account both off-axis distance and thickness [34, 35]. The attenuation coefficient is then not sensitive to the individual measurements but described by the parameters of the model.

Pencil beam scatter kernels

The scattered dose is estimated with the superposition of the scatter kernels. The scatter kernels are derived experimentally from measurements. Because the generation of a pencil beam is not possible, a work-around method is presented. The ultimate verification of the derived kernels is by comparing the derived kernels with Monte Carlo simulations[1]. In literature, these kernels are described f.e. by Hansen et al [26] or by McCurdy et al [30]. A direct comparison with these two publications is however not straightforward because the scatter kernels derived here are measured under full scatter conditions while in literature often only photon fluence is described. The conversion from photon fluence to dose is not trivial because the energy of the scattered photon has to be taken into account. Measurements presented in this report are performed under full scatter conditions in a water tank, this makes a comparison with literature difficult. Because of the considerations mentioned above, no comparison with other studies is done.

Another possibility to improve the pencil beam scatter kernels, other than Monte Carlo simulations, is to derive an analytical function to describe the scatter kernel. With such an analytical model it is possible to fit the measurements for all the phantom thicknesses to a scatter kernel function, and not only fit the kernel function to one particular phantom thickness as is done in this report. The magnitude and half width at half maximum for the different phantom thicknesses can be explained qualitatively but to cast these observations in a mathematical framework is currently not possible, however there are some first approaches presented in literature [2, 27].

A first attempt to develop an analytical model was shown in this report by fitting the kernels to the Klein-Nishina differential cross section. The Klein-Nishina kernel did not describe the scatter

[1] A Monte Carlo code is currently available at MAASTRO CLINIC, but with this method it is not (yet) possible to simulate a pencil beam. Also the separation between primary and scattered dose was not possible.

kernel accurate. There are several reasons for this. First, the Klein-Nishina kernel assumes that photons only scatter once. This is an approximation that is correct for thin phantoms. However for thicker phantoms, the higher order scatter becomes more important and can account for another 20% of the scatter signal for a 6 MV beam [27]. Second, the Klein-Nishina cross-section only predicts the direction of the scattered photon; the energy of the scattered photon also depends on this correction. This energy is important because the scatter is measured not as a photon fluence counter but as dose measured under full scatter conditions in a water phantom [2]. Third, the mean energy of the photon beam is not constant. Beam hardening will occur for larger phantom thicknesses, which results in a higher mean energy. The Klein-Nishina differential cross section decreases for higher photon energies, resulting in a decrease in width of the scatter kernel. So if the mean energy is a function of the phantom thickness, the decrease in width of the kernel for larger phantom thicknesses can be taken into account. If the presented improvements above of the model are taken into account, then the dose prediction model with the Klein-Nishina kernel can improve.

The use of the EHP and pencil beam concept

The pencil beams derived for other air gaps show that the kernels can be scaled with divergence as if the scatter is created at the center-of-mass of the phantom. This is in agreement with other Monte Carlo studies [26]. This property of the scatter kernels is the justification of the use of the equivalent homogeneous phantom for the prediction of the scattered dose in the portal image.

The model uses the pencil beam concept for the prediction of the scattered dose in the portal image. The scatter kernel used is the same for the on- and off-axis locations. This is an assumption that is not strictly true because the amount of scatter that is created at a fixed distance behind the phantom depends in the first place on the thickness of the phantom but second also on the energy spectrum of the photon beam. This photon beam has a lower energy off-axis (beam softening) so a higher amount of scatter will be created at the off-axis points. This second property is however very small. The use of different pencil beam scatter kernels for the off-axis locations is, based on the results of the phantom study, not necessary.

The model predicts the dose based on the hypothesis that the pencil beam scatter only depends on the radiological thickness and the distance of the center-of-mass along the ray line. Because the scatter kernel is assumed to be radial symmetric, this is not necessarily true for highly inhomogeneous densities. These inhomogeneities can break the radial symmetry and the kernel is then not a good representation of the scatter. However, this asymmetry only occurs for multiple scattered photons inside the medium in the region of high electron density gradients. The majority of the scattered photons that are detected are single scattered photons [27]. So the representation of the superposition of the incident beam with pencil beams remains valid in this case.

Because the calculations and measurements are performed numerically with discrete data points, the resolution of the grid size can be of importance. The incident pencil beam grid is scaled to the dimensions of the portal dose grid. This grid is fixed as a result of the pixel size in the EPID after the corrections from grayscale values to dose are made; the pixel spacing is 3.1 mm. McCurdy et al [4] estimated the dependency of the dose grid on the accuracy of the prediction by means of Monte Carlo simulations and found that a grid size of 5 mm was sufficient. A larger grid resulted in larger errors of the prediction and a smaller grid only increased the computation time and did not increase the accuracy. The grid size used in this report is 3.1 mm. So no effects of the grid size on the accuracy of the prediction model are expected.

Overal accuracy of the model

The overal accuracy of the model for the prediction of the portal dose is estimated through various phantom measurements. The accuracy of the model does not depend on the field size, or on the field symmetry. For phantoms, either homogeneous or highly inhomogeneous, the accuracy is estimated to be within 2% of the measured dose. This is true if the center-of-mass of the phantom

is located at the isocenter plane. Deviations from this criterion result in a larger error that can be estimated by a simple rule of thumb.

Further improvements of the model

The model presented here is only fitted to a clinical 6 MV photon beam. The linear accelerators used currently at MAASTRO CLINIC, Elekta SL15s, also produce a 10 MV photon beam. This photon energy was not investigated in this report because the physics describing the interaction processes are more or less the same. The results from this model can also be used for a 10 MV beam. In fact, the scatter produced by a 10 MV beam in general decreases for higher photon energies, so the 6 MV is most suitable to test the prediction model. The differences of the model for a 10 MV instead of a 6 MV beam will be a smaller attenuation coefficient and the scatter kernels will have a lower magnitude and smaller width.

The possible use of a wedge is also not implemented in the model. The use of static wedge extends the prediction model. The attenuation coefficient of the model must be adjusted slightly to incorporate the beam hardening effects that occur in a static wedge, see [25]. For the implementation of a virtual wedge there are no modifications of the model necessary because the wedge is produced by a difference in fluence created by a moving collimator jaw.

Extraction of radiological thickness

Another feature of the model is the iteratively reconstruction of the radiological thickness, see section 4.5. The input for this reconstruction is the open beam dose profile and the measured dose profile. To make a comparison with the prediction model, the radiological thickness of phantom C is extracted based on the open and the measured dose distributions. The results of this radiological thickness extraction are shown in figure 7.1.

The radiological thickness, expressed as polystyrene equivalent thickness, can be extracted with an accuracy generally below 5 mm, excluding the regions of steep dose gradients. This maximum difference of 5 mm is related to a maximum dose difference[2] of $\pm 1\%$. If the measured dose distribution is used without a correction for the scattered dose then the radiological thickness is underestimated up to 3 cm. This would result in an overestimation of the primary dose up to 8%.

The model iteratively reconstructs the radiological thickness which is directly related to the primary dose. An advantage of the superposition with the scatter kernels is that the scattered dose in the portal image has no steep gradients in the dose and is a slowly varying function of the phantom properties and off axis location. This is an advantage if the model is used to calculate the radiological thickness iteratively; the solution will converge to a stable solution within a few iteration steps. Most of the time 2 or 3 iteration loops are sufficient [36]. The extraction of the thickness in figure 7.1 is done with only two iteration loops.

The extraction of the primary dose is more interesting than the extraction of the radiological thickness. The primary dose is input for the three-dimensional dose reconstruction as described in chapter 1 but can also be used to correct for scatter in the images obtained by a cone beam CT scan. This leads to a better reconstruction of the CT data / electron density map as described by [36].

Furthermore, the model can be used to extract the incident beam profile from the measured portal image and the CT scan. This can be a valuable tool for the evaluation of intensity modulated radiation treatment (IMRT) fields during treatment [32].

[2] Primary transmission T^P is related to radiological thickness t through the attenuation coefficient μ. Difference in primary transmission ΔT^P is related to difference in radiological thickness Δt: $T^P = \exp(-\mu t) \rightarrow \frac{dT^P}{dt} = -\mu \exp(-\mu t) \rightarrow \Delta T^P = -\mu \exp(-\mu t) \cdot \Delta t$.

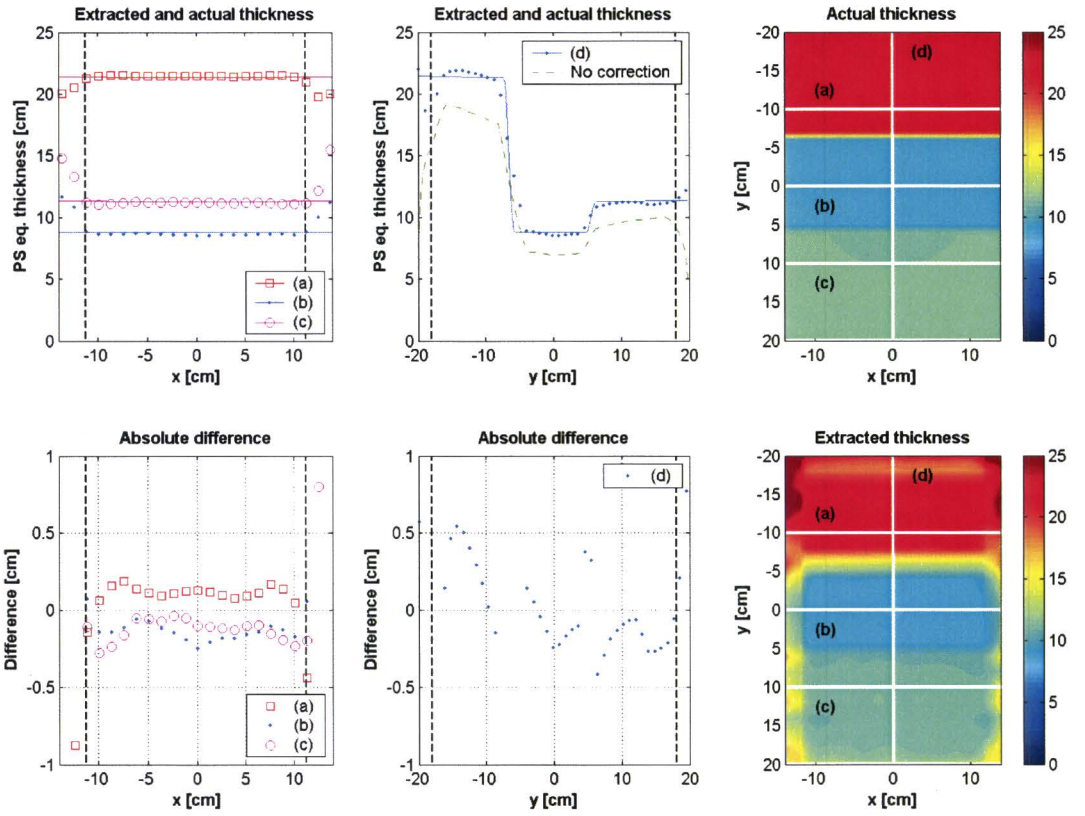

Figure 7.1: The results of the iterative reconstruction of the radiological thickness. In the upper and lower right plot the actual and reconstructed thickness are shown, respectively. The upper two plots on the left show some cross sections with the actual and reconstructed thickness, the solid lines are the actual thicknesses and the measurements are indicated with a symbol, the dash-dot line in the upper middle plot shows the thickness if not the primary dose but the total dose is used for the thickness estimation. Below these plots the absolute differences between extracted and actual thickness are shown. The vertical dashed lines indicate the field edges.

Conclusion

The described model in this report is able to predict the dose behind a phantom/patient in a portal image based on the open beam dose distributions and a map of the radiological thickness of the phantom/patient. The accuracy of the model is better than 2% if the center-of-mass of the phantoms/patients is located at the isocenter plane. Deviations from this center-of-mass criterium results in an approximation of the predicted dose and the error can be estimated in advance by taking the displacement of the center-of-mass and the radiological thickness into account.

The problem with comparing treatment-time portal images with predicted portal images is that if there are deviations between these distribution the clinical importance is not easy to interpret. Deviations can f.e. occur due to a different patient set-up, incorrect dosimetric performance of the linear accelerator or difference in patient anatomy (organ motion) [5]. The full gain of the acquirement of the portal dose images can be achieved by developing a way to relate this dose to specific points inside the patient. There are some studies [11, 37] describing such methods but finally a three-dimensional dose reconstruction will be the ultimate goal [13, 14]. Before this can be achieved, a detailed analysis of the dose in the portal image has to be made. This report describes this analysis, so the first step towards three-dimensional dose reconstruction is successfully made.

References

[1] M. Essers and B.J. Mijnheer. In vivo dosimetry during external photon beam radiotherapy. *Int. J. Radiat. Oncol. Biol. Phys.*, 43(2):245–259, 1999.

[2] L. Spies, P.M. Evans, M. Partridge, V.N. Hansen, and T. Bortfeld. Direct measurement and analytical modeling of scatter in portal imaging. *Med. Phys.*, 27(3):462–471, 2000.

[3] K.L. Pasma, B.J.M. Heijmen, M. Kroonwijk, and A.G. Visser. Portal dose image (PDI) prediction for dosimetric treatment verification in radiotherapy. I. An algorithm for open beams. *Med. Phys.*, 25(6):830–840, 1998.

[4] B.M.C. McCurdy and S. Pistorius. Photon scatter in portal images: Accuracy of a fluence based pencil beam superposition algorithm. *Med. Phys.*, 27(5):913–922, 2000.

[5] M. Kroonwijk, K.L. Pasma, S. Quint, P.C.M. Koper, A.G. Visser, and Heijmen B.J.M. In vivo dosimetry for prostate cancer patients using an electronic portal imaging device (EPID); demonstration of internal organ motion. *Radiother. Oncol.*, 49:125–132, 1998.

[6] R. Boellaard, M. van Herk, and B. Mijnheer. A convolution model to convert transmission dose images to exit dose distributions. *Med. Phys.*, 24(2):189–199, 1997.

[7] R. Boellaard, M. van Herk, H. Uiterwaal, and B. Mijnheer. Two-dimensional exit dosimetry using a liquid-filled electronic portal imaging device and a convolution model. *Radiother. Oncol.*, 44:149–157, 1997.

[8] R. Bogaerts, D. Huyskens, C. Weltens, and A. Dutreix. Variation of relative transit dose profiles with patient-detector distance. *Radiother. Oncol.*, 54:29–37, 2000.

[9] D. Huyskens, J. van Dam, and A. Dutreix. Midplane dose determination using in vivo dose measurements in combination with portal imaging. *Phys. Med. Biol.*, 39:1089–1101, 1994.

[10] R. Boellaard, M. Essers, M. van Herk, and B.J. Mijnheer. New method to obtain the midplane dose using portal in vivo dosimetry. *Int. J. Radiat. Oncol. Biol. Phys.*, 41(2):465–474, 1998.

[11] R. Boellaard, M. van Herk, H. Uiterwaal, and B. Mijnheer. First clinical tests using a liquid-filled electronic portal imaging device and a convolution model for the verification of the midplane dose. *Radiother. Oncol.*, 47:303–312, 1998.

[12] V.N. Hansen, P.M. Evans, and W. Swindell. The application of transit dosimetry to precision radiotherapy. *Med. Phys.*, 23(5):713–721, 1996.

[13] M. Partridge, M. Ebert, and B-M. Hesse. IMRT verification by three-dimensional dose reconstruction from portal beam measurements. *Med. Phys.*, 29(8):1847–1858, 2002.

[14] R.J.W. Louwe, E.M.F. Damen, M. van Herk, A.W.H. Minken, O. Torzsok, and B.J. Mijnheer. Three-dimensional dose reconstruction of breast cancer treatment using portal imaging. *Med. Phys.*, 30(9):2376–2389, 2003.

[15] F.M. Khan. *The Physics of Radiation Therapy.* Lippencott Williams & Wilkins, Third edition, ISBN 0-7817-3065-1, 2003.

[16] P. Metcalfe, T. Kron, and P. Hoban. *The Physics of Radiotherapy X-Rays from Linear Accelerators.* Medical Physics Publishing, Madison, Wisconsin, Second Printing edition, ISBN 0-9448-3876-6, 2002.

[17] K.S. Krane. *Introductory Nuclear Physics.* John Wiley & Sons, New York, First edition, ISBN 0-4718-0533-X, 1988.

[18] A.L. Boyer, L. Antonuk, A. Fenster, M. van Herk, H. Meertens, P. Munro, L.E. Reinstein, and J. Wong. A review of electronic portal imaging devices (EPIDs). *Med. Phys.*, 19(1):1–16, 1992.

[19] B.J.M. Heijmen, K.L. Pasma, M. Kroonwijk, V.G.M. Althof, J.C.J. de Boer, A.G. Visser, and H. Huizinga. Portal dose measurements in radiotherapy using an electronic portal imaging device. *Phys. Med. Biol.*, 40(11):1943–1955, 1995.

[20] C. Peters. *Transmissiedosimetrie m.b.v. MegaVolt Imaging binnen het RTIL.* FIK/KFM 2000-01, Eindhoven University of Technology, 2000.

[21] S.M.J.J.G. Nijsten, A.W.H. Minken, P. Lambin, and I.A.D. Bruinvis. Verification of treatment parameter transfer by means of electronic portal dosimetry. *Med. Phys.*, 31(2):341–347, 2004.

[22] S.M.J.J.G. Nijsten. *Electronic Portal Imaging: Quality Assurance bij Radiotherapie.* Stan Ackermans Institute, Eindhoven University of Technology, ISBN 90-444-0145-9, 2001.

[23] V.G.M. Althof, J.C.J. de Boer, H. Huizinga, and A.G. Visser. Physical characteristics of a commercial electronic portal imaging device. *Med. Phys.*, 23(11):1845–1855, 1996.

[24] D.A. Jaffray, J.J. Battista, A. Fenster, and P. Munro. X-ray scatter in megavoltage transmission radiography: Physical characteristics and influence on image quality. *Med. Phys.*, 21(1):45–60, 1994.

[25] K.L. Pasma, Quint S.C., and B.J.M. Heijmen. Portal dose image prediction for dosimetric treatment verification in radiotherapy. II. An algorithm for wedged beams. *Med. Phys.*, 29(6):925–931, 2002.

[26] V.N. Hansen, W. Swindell, and P.M. Evans. Extraction of pimary signal from EPID's using only forward convolution. *Med. Phys.*, 24(9):1477–1484, 1997.

[27] L. Spies and T. Bortfeld. Analytical scatter kernels for portal imaging at 6MV. *Med. Phys.*, 28(4):553–559, 2001.

[28] W. Swindell and P.M. Evans. Scattered radiation in portal images: A Monte Carlo simulation and a simple physical model. *Med. Phys.*, 23(1):63–73, 1996.

[29] M. Fippel. Fast Monte Carlo dose calculation for photon beams based on the VMC electron algorithm. *Med. Phys.*, 26(8):1466–1475, 1999.

[30] B.M.C. McCurdy and S. Pistorius. Photon scatter in portal images: Physical characteristics of pencil beam kernels generated using the EGS Monte Carlo code. *Med. Phys.*, 27(2):312–320, 2000.

[31] A. Ahnesjo, M. Saxner, and A. Trepp. A pencil beam model for photon dose calculation. *Med. Phys.*, 19(2):263–273, 1992.

[32] L. Spies, M. Partridge, B.A. Groh, and T. Bortfeld. An iterative algorithm for reconstructing incident beam distributions from transmission measurements using electronic portal imaging. *Phys. Med. Biol.*, 46(8):N203–N211, 2001.

[33] E.J. Morton, W. Swindell, D.G. Lewis, and P.M. Evans. A linear array, scintillation crystal-photodiode for megavoltage imaging. *Med. Phys.*, 18(4):681–691, 1991.

[34] M.K. Yu, R.S. Sloboda, and B. Murray. Linear accelerator photon beam quality at off-axis points. *Med. Phys.*, 24(2):233–239, 1997.

[35] C. Kleinschmidt. Analytical considerations of beam hardening in medical accelerator photon spectra. *Med. Phys.*, 26(9):1995–1999, 1999.

[36] L. Spies, M. Ebert, B.A. Groh, B.M. Hesse, and T. Bortfeld. Correction of scatter in megavolt conebeam CT. *Phys. Med. Biol.*, 46(3):821–833, 2001.

[37] K.L. Pasma, M. Kroonwijk, Quint S., A.G. Visser, and B.J.M. Heijmen. Transit Dosimetry with an electronic portal imaging device (EPID) for 115 prostate cancer patients. *Int. J. Radiat. Oncol. Biol. Phys.*, 45(5):1297–1303, 1999.

[38] D.A. Low and J.F. Dempsey. Evaluation of the gamma dose distribution comparison method. *Med. Phys.*, 30(9):2455–2464, 2003.

[39] D.A. Low, W.B. Harms, S. Mutic, and J.A. Purdy. A technique for the quantitative evaluation of dose distributions. *Med. Phys.*, 25(5):656–661, 1998.

Appendix A

Semi-Analytical Derivation of the Pencil Beam Scatter Kernels

The method described here to derive the pencil beam scatter kernels (PBSK) is semi-analytical. This derivation is not used because of the time consuming procedures needed to perform the measurements: circular blocks have to be made out of cerroband to create circular fields. The blocks are attached to a tray and for measurement of a different field size the tray has to be replaced.

The on-axis transmission values $T(A,t)$ through homogeneous phantoms with radiological thickness t, irradiated with a circular field with area A can be fitted to a polynomial. The coefficients of the polynomial characterize the PBSK. Fitting the transmission values to a polynomial of N'th order:

$$\begin{aligned} T(A,t) &= T^P(t) + T^S(A,t) \\ &= a_0(t) + a_1(t)A + a_2(t)A^2 + \cdots + a_N(t)A^N = \sum_{n=0}^{N} a_n(t)A^n. \end{aligned} \tag{A.1}$$

The coefficients $a_n(t)$ are related to physical parameters; $a_0(t)$ is the primary transmission $T^P(t)$ and is related to the effective attenuation coefficient μ

$$T^P(t) = a_0(t) = e^{-\mu t}, \tag{A.2}$$

the coefficients $a_1(t), \ldots, a_N(t)$ are related to the scattered transmission $T^S(A,t)$, using $A = \pi r^2$:

$$\begin{aligned} T^S(A,t) &= a_1(t)A + a_2(t)A^2 + \cdots = a_1(t)\pi r^2 + a_2(t)(\pi r^2)^2 + \cdots \\ &= \sum_{n=1}^{N} a_n(t)A^n = \int_0^r 2\pi \frac{O(r')}{O(0)} K(t,r')r'dr', \end{aligned} \tag{A.3}$$

with $O(r)$ the open beam dose profile and $K(t,r)$ the PBSK. This PBSK can be analytically derived by differentiating the left and the right side of eq. (A.3):

$$\frac{dT^S(A,t)}{dr} = a_1(t)2\pi r + a_2(t)4\pi^2 r^3 + \cdots = \frac{O(r)}{O(0)} K_t(r)2\pi r, \tag{A.4}$$

rewriting eq. (A.4) yields

$$\begin{aligned} K(t,r) &= \frac{O(0)}{O(r)}\left(a_1(t) + a_2(t)2\pi r^2 + \cdots\right) = \frac{O(0)}{O(r)}\sum_{n=1}^{N} n a_n(t)[\pi r^2]^{n-1} \\ &= \frac{O(0)}{O(r)}\sum_{n=1}^{N} n a_n(t) A^{n-1}. \end{aligned} \tag{A.5}$$

The PBSK for a particular thickness t can be derived from the coefficients $a_n(t)$ of the polynomial fit through the on-axis transmission measurements for various field sizes.

Appendix B

Measurement Data

In this appendix the raw measurement data from the various point measurements are shown as well as some figures representing this data. For an explanation of the tables and the figures see the text of the corresponding chapter.

Table B.1: On- and off-axis measured transmission for the derivation of the attenuation coefficient.

Field size [cm×cm]	Off-axis distance [cm]	Polystyrene thickness 4.3 cm [-]	8.6 cm [-]	12.9 cm [-]	17.1 cm [-]	21.4 cm [-]
3×3	0.0	0.7945	0.6527	0.5384	0.4473	0.3730
4×4	0.0	0.7955	0.6527	0.5386	0.4481	0.3739
5×5	0.0	0.7951	0.6530	0.5405	0.4487	0.3749
3×3	3.0	0.7975	0.6537	0.5383	0.4470	0.3721
4×4	3.0	0.7979	0.6539	0.5389	0.4472	0.3728
5×5	3.0	0.7979	0.6537	0.5396	0.4485	0.3744
3×3	6.0	0.7950	0.6490	0.5343	0.4414	0.3671
4×4	6.0	0.7951	0.6489	0.5337	0.4416	0.3673
5×5	6.0	0.7954	0.6493	0.5339	0.4425	0.3681
3×3	9.0	0.7915	0.6422	0.5261	0.4337	0.3593
4×4	9.0	0.7905	0.6419	0.5251	0.4342	0.3596
5×5	9.0	0.7907	0.6422	0.5271	0.4347	0.3607

Note that the point measurements for the open beam are taken without the treatment couch in the beam. The other measurements are taken with a phantom placed on this couch, to correct for this difference the factor 0.9778 has to be taken into account, this factor has to be multiplied with the measurement of the open beam to yield the result that would have been acquired with a couch in place. This to compare the results with the other measurements done in this report.

Table B.2: On-axis point measurements for the derivation of the pencil beam scatter kernel. Values are expressed as on-axis transmission. With treatment couch in the beam for measurement of the open beam.

Field size [cm×cm]	Polystyrene thickness 4.3 cm [-]	8.6 cm [-]	12.9 cm [-]	17.1 cm [-]	21.4 cm [-]
3×3	0.8155	0.6706	0.5533	0.4593	0.3831
6×6	0.8174	0.6720	0.5568	0.4633	0.3875
10×10	0.8208	0.6795	0.5661	0.4742	0.3995
15×15	0.8274	0.6937	0.5829	0.4934	0.4199
21×21	0.8370	0.7132	0.6095	0.5227	0.4513
24×24	0.8450	0.7255	0.6220	0.5389	0.4684

Table B.3: Parallel approach: Fitted kernel parameters for the various functions.

	Isotropic			Gaussian			Klein Nishina	
Thickness [cm]	c_1 [-]	c_2 [cm]	c_3 [-]	c_1 [-]	c_2 [cm^{-2}]	c_3 [cm^{-2}]	c_1 [-]	c_2 [-]
4.3	0.8155	61.45	0.1949	0.8155	$1.046 \cdot 10^{-4}$	$0.503 \cdot 10^{-4}$	0.8150	0.1521
8.6	0.6688	28.27	0.0912	0.6688	$1.683 \cdot 10^{-3}$	$1.135 \cdot 10^{-4}$	0.6685	0.2969
12.9	0.5509	24.97	0.0904	0.5509	$2.139 \cdot 10^{-3}$	$1.442 \cdot 10^{-4}$	0.5509	0.3623
17.1	0.4576	24.61	0.1040	0.4576	$2.155 \cdot 10^{-3}$	$1.700 \cdot 10^{-4}$	0.4579	0.4266
21.4	0.3811	23.06	0.1004	0.3812	$2.410 \cdot 10^{-3}$	$1.864 \cdot 10^{-4}$	0.3814	0.4574

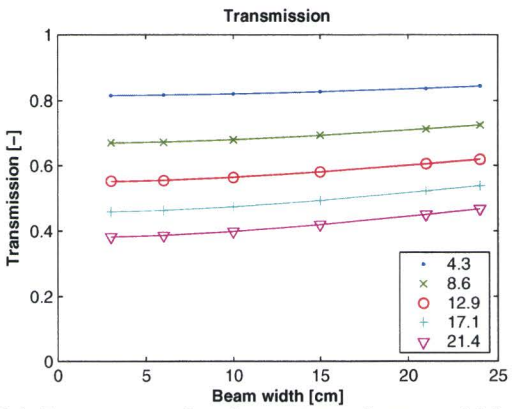

(a) Transmission for the various phantom thicknesses as a function of the field size.

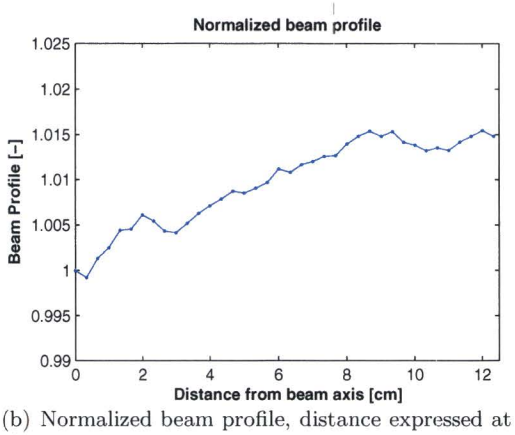

(b) Normalized beam profile, distance expressed at the isocenter.

Figure B.1: Total transmission $T(A,t)$ vs. beam width (a) and the normalized beam profile (b).

Table B.4: Tilted approach: Fitted kernel parameters for the various functions.

	Isotropic			Gaussian			Klein Nishina	
Thickness [cm]	c_1 [-]	c_2 [cm]	c_3 [-]	c_1 [-]	c_2 [cm^{-2}]	c_3 [cm^{-2}]	c_1 [-]	c_2 [-]
4.3	0.8155	104.93	0.2508	0.8155	$4.618 \cdot 10^{-5}$	$2.235 \cdot 10^{-5}$	0.8144	0.0825
8.6	0.6688	42.42	0.0913	0.6688	$7.477 \cdot 10^{-4}$	$5.043 \cdot 10^{-5}$	0.6673	0.1612
12.9	0.5509	37.47	0.0905	0.5516	$9.496 \cdot 10^{-4}$	$6.408 \cdot 10^{-5}$	0.5494	0.1968
17.1	0.4576	36.93	0.1040	0.4576	$9.575 \cdot 10^{-4}$	$7.556 \cdot 10^{-5}$	0.4558	0.2318
21.4	0.3811	34.60	0.1004	0.3812	$1.071 \cdot 10^{-3}$	$8.285 \cdot 10^{-5}$	0.3795	0.2486

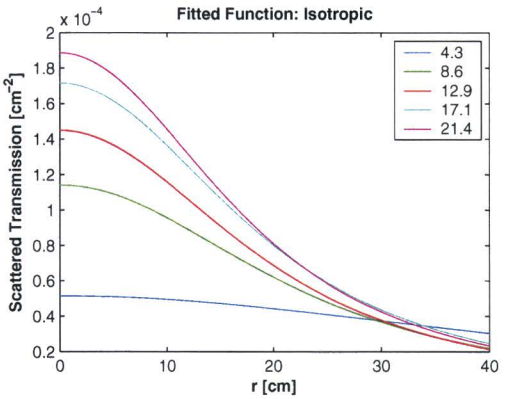

(a) Isotropic kernel.

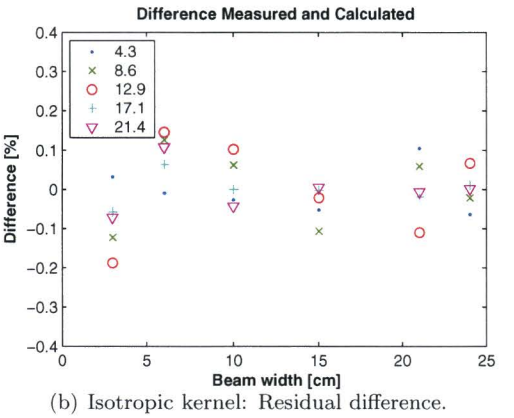

(b) Isotropic kernel: Residual difference.

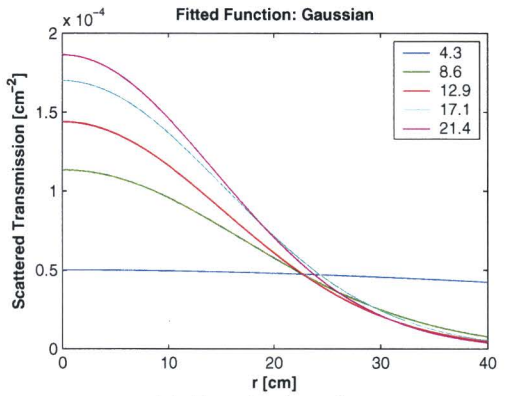

(c) Gaussian kernel.

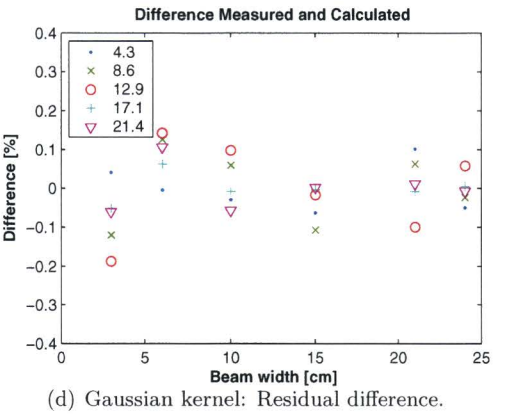

(d) Gaussian kernel: Residual difference.

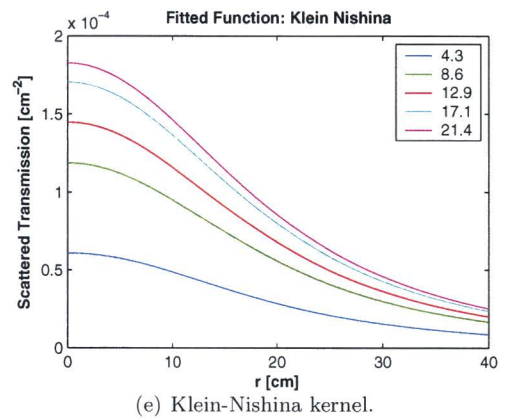

(e) Klein-Nishina kernel.

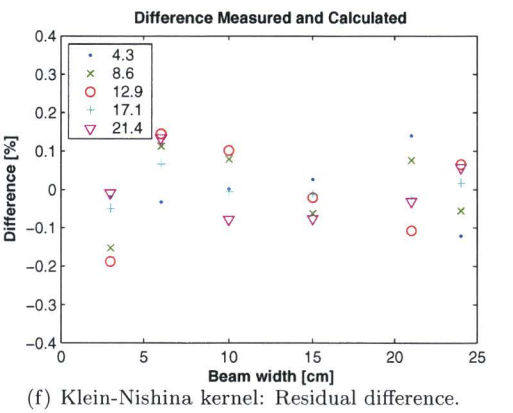

(f) Klein-Nishina kernel: Residual difference.

Figure B.2: Parallel approach: Fitted kernels (left) and the residual difference of the measurements from the fit (right) expressed as a percentage.

Table B.5: On-axis calculated and measured transmission for the parallel and the tilted approach and for the three fitted kernels. Open beam with treatment couch in the beam.

Field size x×y [cm×cm]	Thick-ness [cm]	Measured [-]	Tilted Kernels			Parallel Kernels		
			Gaussian [-]	Isotropic [-]	Klein-Nishina [-]	Gaussian [-]	Isotropic [-]	Klein-Nishina [-]
5×20	4.3	0.8213	0.8177	0.8178	0.8190	0.8175	0.8178	0.8183
10×20	4.3	0.8282	0.8229	0.8230	0.8252	0.8225	0.8230	0.8240
20×5	4.3	0.8223	0.8177	0.8178	0.8190	0.8175	0.8178	0.8183
20×10	4.3	0.8271	0.8229	0.8230	0.8252	0.8225	0.8230	0.8240
5×20	8.6	0.6780	0.6784	0.6784	0.6800	0.6784	0.6784	0.6786
10×20	8.6	0.6904	0.6892	0.6892	0.6920	0.6892	0.6892	0.6897
20×5	8.6	0.6807	0.6784	0.6784	0.6800	0.6784	0.6784	0.6786
20×10	8.6	0.6900	0.6892	0.6892	0.6920	0.6892	0.6892	0.6897
5×20	12.9	0.5662	0.5635	0.5635	0.5649	0.5635	0.5635	0.5632
10×20	12.9	0.5797	0.5775	0.5775	0.5800	0.5775	0.5775	0.5770
20×5	12.9	0.5666	0.5635	0.5635	0.5649	0.5635	0.5635	0.5632
20×10	12.9	0.5792	0.5775	0.5775	0.5800	0.5775	0.5775	0.5770
5×20	17.1	0.4743	0.4730	0.4731	0.4750	0.4730	0.4731	0.4730
10×20	17.1	0.4898	0.4889	0.4889	0.4923	0.4889	0.4890	0.4889
20×5	17.1	0.4747	0.4730	0.4731	0.4750	0.4730	0.4731	0.4730
20×10	17.1	0.4892	0.4889	0.4889	0.4923	0.4889	0.4890	0.4889
5×20	21.4	0.3993	0.3981	0.3981	0.3999	0.3981	0.3981	0.3978
10×20	21.4	0.4156	0.4153	0.4153	0.4184	0.4153	0.4153	0.4148
20×5	21.4	0.3998	0.3981	0.3981	0.3999	0.3981	0.3981	0.3978
20×10	21.4	0.4157	0.4153	0.4153	0.4184	0.4153	0.4153	0.4148

Table B.6: Measured and calculated off-axis transmission for a 5×24 cm^2 field for the three kernels. Open beam without treatment couch in the beam.

Off-Axis Distance [cm]	Thick-ness [cm]	Measured [-]	Kernel Tilting approach			Parallel approach		
			Gaussian [-]	Isotropic [-]	Klein Nishina [-]	Gaussian [-]	Isotropic [-]	Klein Nishina [-]
0.0	4.3	0.8014	0.8006	0.8006	0.8017	0.8006	0.8006	0.8011
0.0	8.6	0.6644	0.6652	0.6652	0.6666	0.6652	0.6652	0.6654
0.0	12.9	0.5532	0.5526	0.5526	0.5510	0.5526	0.5526	0.5526
0.0	17.1	0.4645	0.4652	0.4652	0.4669	0.4652	0.4652	0.4652
0.0	21.4	0.3915	0.3920	0.3921	0.3937	0.3920	0.3921	0.3918
3.0	4.3	0.8044	0.8034	0.8035	0.8044	0.8034	0.8035	0.8038
3.0	8.6	0.6643	0.6663	0.6663	0.6675	0.6661	0.6661	0.6663
3.0	12.9	0.5527	0.5529	0.5530	0.5543	0.5527	0.5527	0.5527
3.0	17.1	0.4636	0.4642	0.4642	0.4658	0.4638	0.4639	0.4639
3.0	21.4	0.3901	0.3903	0.3904	0.3918	0.3899	0.3900	0.3898
6.0	4.3	0.8004	0.8007	0.8007	0.8012	0.8007	0.8006	0.8005
6.0	8.6	0.6587	0.6606	0.6607	0.6615	0.6599	0.6600	0.6599
6.0	12.9	0.5461	0.5489	0.5490	0.5499	0.5479	0.5480	0.5480
6.0	17.1	0.4562	0.4579	0.4581	0.4591	0.4567	0.4569	0.4569
6.0	21.4	0.3840	0.3850	0.3851	0.3861	0.3835	0.3838	0.3837
9.0	4.3	0.7969	0.7976	0.7976	0.7975	0.7976	0.7974	0.7966
9.0	8.6	0.6507	0.6532	0.6533	0.6535	0.6517	0.6520	0.6517
9.0	12.9	0.5368	0.5385	0.5387	0.5389	0.5363	0.5368	0.5367
9.0	17.1	0.4470	0.4491	0.4493	0.4496	0.4465	0.4470	0.4470
9.0	21.4	0.3745	0.3754	0.3757	0.3760	0.3724	0.3730	0.3732

Table B.7: Measured and calculated off-axis transmission for a 15×24 cm^2 field for the three kernels. Open beam without treatment couch in the beam.

Off-Axis Distance [cm]	Thickness [cm]	Measured [-]	Kernel Tilting approach			Parallel approach		
			Gaussian [-]	Isotropic [-]	Klein Nishina [-]	Gaussian [-]	Isotropic [-]	Klein Nishina [-]
0.0	4.3	0.8178	0.8127	0.8128	0.8146	0.8127	0.8128	0.8137
0.0	8.6	0.6891	0.6895	0.6895	0.6919	0.6895	0.6895	0.6899
0.0	12.9	0.5847	0.5825	0.5825	0.5849	0.5825	0.5825	0.5825
0.0	17.1	0.4995	0.5005	0.5005	0.5033	0.5005	0.5005	0.5004
0.0	21.4	0.4295	0.4300	0.4301	0.4327	0.4300	0.4301	0.4296
3.0	4.3	0.8202	0.8155	0.8156	0.8170	0.8155	0.8155	0.8159
3.0	8.6	0.6887	0.6902	0.6902	0.6922	0.6896	0.6897	0.6899
3.0	12.9	0.5833	0.5823	0.5824	0.5844	0.5815	0.5816	0.5816
3.0	17.1	0.4978	0.4988	0.4989	0.5012	0.4978	0.4980	0.4979
3.0	21.4	0.4268	0.4275	0.4276	0.4299	0.4263	0.4266	0.4263
6.0	4.3	0.8145	0.8126	0.8126	0.8130	0.8126	0.8123	0.8114
6.0	8.6	0.6818	0.6835	0.6836	0.6845	0.6813	0.6817	0.6813
6.0	12.9	0.5748	0.5768	0.5770	0.5780	0.5736	0.5742	0.5741
6.0	17.1	0.4888	0.4907	0.4910	0.4921	0.4870	0.4877	0.4876
6.0	21.4	0.4186	0.4201	0.4205	0.4215	0.4157	0.4166	0.4167
9.0	4.3	0.8086	0.8095	0.8093	0.8080	0.8093	0.8086	0.8060
9.0	8.6	0.6717	0.6746	0.6749	0.6740	0.6703	0.6711	0.6701
9.0	12.9	0.5634	0.5642	0.5648	0.5640	0.5579	0.5593	0.5591
9.0	17.1	0.4770	0.4793	0.4800	0.4791	0.4718	0.4734	0.4734
9.0	21.4	0.4063	0.4075	0.4084	0.4076	0.3989	0.4008	0.4015

Appendix C

Gamma Method

In radiotherapy, the criteria for dose delivery is that the actual delivered dose is within 3% of the planned dose, for areas with steep dose gradients this criterion is replaced by the criterion that the planned dose must be within 3 mm of the delivered dose. This requires two verification methods for dose distributions, however a single method is developed to combine these two criteria, the so-called gamma method [38, 39].

The gamma method is based on both dosimetric and spatial differences. The gamma function $\Gamma(\mathbf{r}_1, \mathbf{r}_2)$ is defined as

$$\Gamma(\mathbf{r}_1, \mathbf{r}_2) = \sqrt{\frac{r^2(\mathbf{r}_1, \mathbf{r}_2)}{\Delta d_M^2} + \frac{\delta^2(\mathbf{r}_1, \mathbf{r}_2)}{\Delta D_M^2}}, \tag{C.1}$$

with $r(\mathbf{r}_1, \mathbf{r}_2) = |\mathbf{r}_1 - \mathbf{r}_2|$ the pathlength difference between $\mathbf{r}_1$ and $\mathbf{r}_2$, and $\delta(\mathbf{r}_1, \mathbf{r}_2) = D(\mathbf{r}_1) - D(\mathbf{r}_2)$ the difference between the dose at point $\mathbf{r}_1$ and $\mathbf{r}_2$. The criteria for the maximum dose and pathlength difference are ΔD_M and Δd_M, respectively.

The gamma value $\gamma(\mathbf{r}_1)$ at the specific point $\mathbf{r}_1$ can be calculated by minimizing the gamma function $\Gamma(\mathbf{r}_1, \mathbf{r}_2)$:

$$\gamma(\mathbf{r}_1) = \min\{\Gamma(\mathbf{r}_1, \mathbf{r}_2)\} \forall \{\mathbf{r}_2\} \tag{C.2}$$

In this report, the criteria for the maximum difference are defined as $\Delta D_M = 0.03 \cdot \max\{D(\mathbf{r}_1)\}$ is 3% of the maximum dose, and $\Delta d_M = 5$ mm.

The values of γ that are smaller than 1 have dose differences smaller than 3% or spatial differences smaller than 5 mm.